

Optimizing the nitrogen configuration in interlayer-expanded carbon materials via sulfur-bridged bonds toward remarkable energy storage performances

Zhiqiang Li,^{1Δ} Yang Yang,^{2Δ} Gaohui Ding,^{1Δ} Lingzhi Wei,¹ Ge Yao,¹ Helin Niu,³
Fangcai Zheng*^{1,3} and Qianwang Chen**^{1,2}

¹ Institutes of Physical Science and Information Technology, Key Laboratory of Structure and Functional Regulation of Hybrid Materials, Anhui University, Ministry of Education, Hefei, 230601, People's Republic of China

² Hefei National Laboratory for Physical Science at Microscale and Department of Materials Science & Engineering, University of Science and Technology of China, Hefei 230026, People's Republic of China

³ Key Laboratory of Functional Inorganic Material Chemistry of Anhui Province, Anhui University, Hefei 230601, People's Republic of China

* Corresponding authors: zfc@mail.ustc.edu.cn (F.C. Zheng)

cqw@ustc.edu.cn (Q. W. Chen)

Δ These authors contribute equally to this work.

1. Experimental section

1.1 Material synthesis

1.1.1 Synthesis of Mn-BTC

All chemicals are of analytical grade and were directly used without any further purification. In a typical synthesis procedure, 0.2 mmol of MnCl_2 and 0.3 g of polyvinyl pyrrolidone (PVP) were added to 10 ml of the mixed solution of $\text{C}_2\text{H}_5\text{OH}$ and H_2O (1:1) under stirring until completely dissolved, it is solution A. 90 mg of 1,3,5-benzenetricarboxylic acid were dissolved in 10 ml of the mixed solution of $\text{C}_2\text{H}_5\text{OH}$ and H_2O (1:1), it is solution B. Subsequently, the solution B was regularly added to the solution A with stirring. After 10 min, the resulting solution was incubated at room temperature without interruption for 24 h. The resulting Mn-BTC were collected by centrifugation, washed with ethanol several times, and finally dried in an oven at 60 °C.

1.1.2 Synthesis of CMs

The resulting Mn-BTC nanorods were carbonized at 600 °C for 2 h with a heating rate of 10 °C/min in N_2 . The obtained sample was denoted as $\text{MnO}@C$. $\text{MnO}@C$ Ms was etched by 3M HCl for 12 h, and the corresponding sample was denoted as CMs.

1.1.3 Synthesis of S-CMs

The as-prepared CMs and sulfur powder with a weight ratio of 1:5 were loaded in a ceramic boat, and then transferred to a tubular furnace. The sulfur powder was placed in the upper wind. Subsequently, the furnace heated to 600 °C for 2 h with a ramping rate of 10 °C/min in N_2 , and then was naturally cooled down to room temperature. The obtained sample was denoted as S-CMs.

1.1.4 Synthesis of S/N-CMs

The as-prepared S-CMs was annealed at 600 °C for 2 h with a heating rate of 10 °C/min in NH₃, and then cooled to room temperature. The obtained sample was denoted as S/N-CMs. When the nitridation temperature was setted at 700 °C, the resulting sample was denoted as S/N-CMs-700.

1.1.5 Synthesis of N-CMs

The as-prepared CMs was annealed at 600 °C for 2h with a heating rate of 10 °C/min in NH₃, and then cooled to room temperature. The obtained sample was denoted as N-CMs.

1.1.6 Synthesis of N/S-CMs

The as-prepared N-CMs and sulfur powder with a weight ratio of 1:5 were loaded in a ceramic boat, and then transferred to a tubular furnace. The sulfur powder was placed in the upper wind. Subsequently, the furnace heated to 600 °C for 2h with a ramping rate of 10 °C/min in N₂, and then naturally cooled to room temperature. The obtained sample was denoted as N/S-CMs.

1.2 Material characterization

The crystal phase of all samples was analyzed by a power X-ray diffractometer (SmartLab 9KW) equipped using Cu-K α radiation. The morphologies of the as-prepared samples were investigated using scanning electron microscopy (SEM, JEOL JSM-6700 M) with a voltage of 200 kV and transmission electron microscopy (TEM, Hitachi H-800) using an accelerating voltage of 200 kV. High resolution transmission electron microscopy (HRTEM, JEOL-2011) was further performed to investigate the

structure of the resulting samples. A TGA-5500 thermoanalyser (TGA) was applied to characterize the thermal stability of the Mn-BTC under flowing nitrogen with a heating rate of 10 °C/min. X-ray photoelectron spectroscopy (XPS, ESCALAB 250 Xi) was performed to investigate the chemical valence and components of all elements in the resulting samples. The specific surface area and pore structural characteristics of the resulting carbon materials were measured by a sorption analyzer (Micromeritics ASAP 2020) at 77 K. The Raman spectrum was obtained using a Confocal Laser MicroRaman Spectrometer (Via-Reflex / inVia-Reflex).

1.3 Electrochemical measurements

The as-prepared samples were measured as anode materials for PIBs. The homogeneous slurry was obtained by mixing the as-prepared sample (80 %), polyvinylidene difluoride (PVDF, 10 %), and carbon black (10 %) in N-methyl-2-pyrrolidone (NMP). Finally, the slurry was coated on the copper foil, which was further dried in a vacuum oven at 80 °C overnight. The potassium-storage performances were evaluated using a CR2032 coin-type cell assembled in an argon-filled glove box (MBRAUN UNILAB PRO, SP (1800/780)). The glass fiber (GF/D, Whatman) was used as the separator. The metallic K was used as the counter electrode. The electrolyte is 3M potassium bis(fluorosulfonyl)imide (KFSI) in ethylene carbonate and diethyl carbonate (EC:DEC = 1:1). The mass loading of the electrode materials is about 0.6-0.7 mg. The potassium-storage performance was tested by a galvanostatic charge/discharge technique on a battery testing system (Neware). Cyclic voltammetry (CV) curves were performed on a CHI760E

electrochemical workstation.

1.4 Theoretical calculation

The DFT calculations were performed using the Vienna Ab Initio Simulation Package (VASP) and the generalized gradient approximation (GGA) of Perdew-Becke-Ernzerhof (PBE) is used for the exchange-correlation functional. The cut-off energy was set to 450 eV for the plane-wave expansion of the electronic wave function. A vacuum space of 15 Å was inserted along the z direction to avoid any interactions between the periodically repeated images. All structures were optimized with a convergence criterion of 1×10^{-5} eV for the energy and 0.02 eV/Å for the forces. The k-point mesh of $5 \times 5 \times 1$ was used to represent the Brillouin zone for structure optimization. The adsorption (binding) energy of the K atoms was evaluated from $\Delta E_a = E_{GK} - (E_G + E_K)$ where E_{GK} and E_G are the energies of doped graphene models after K adsorption and without adsorption, respectively. Vander Waals corrections were considered in the calculations of two-layer graphene models.

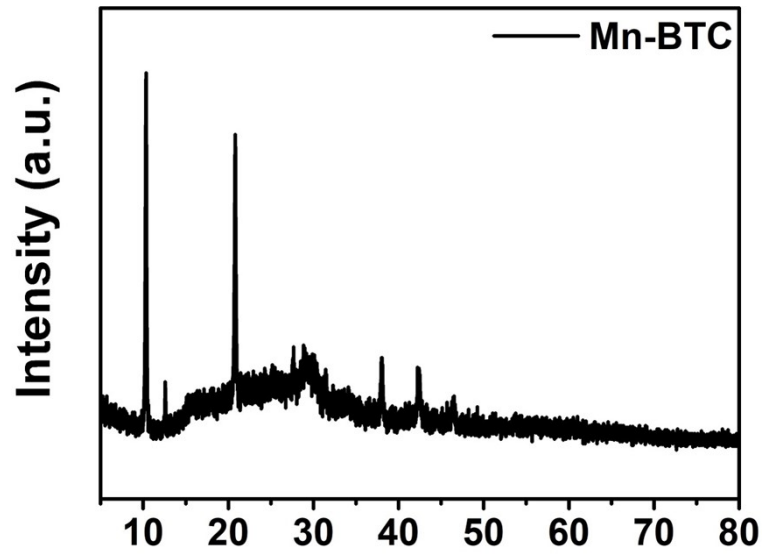


Figure S1. XRD pattern of Mn-BTC.

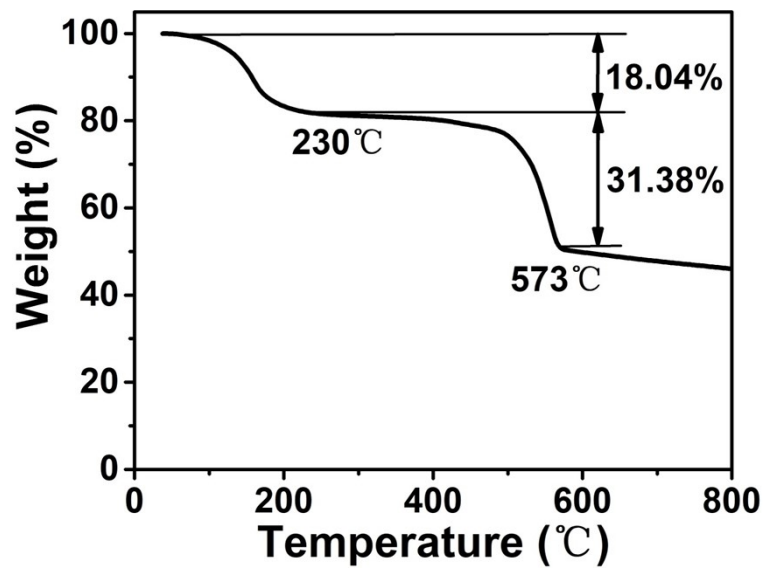


Figure S2. The TGA curve of Mn-BTC in N₂.

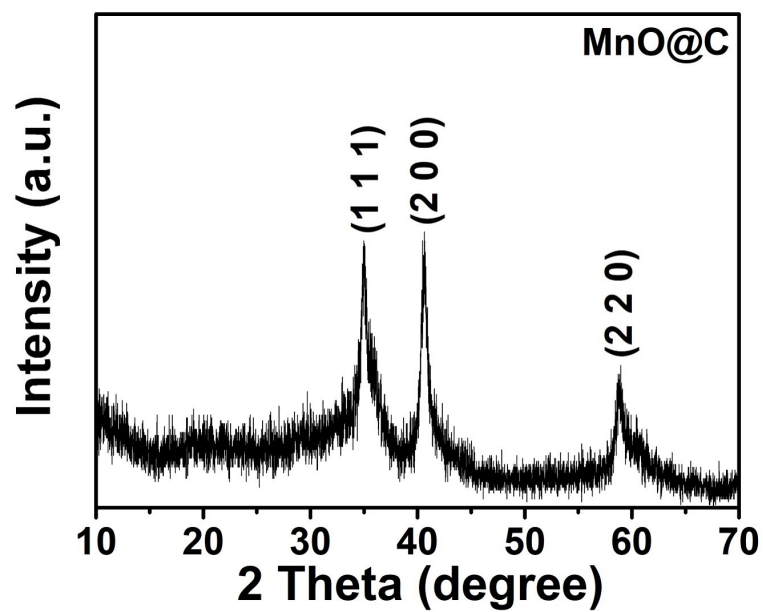


Figure S3. The XRD pattern of MnO@C.

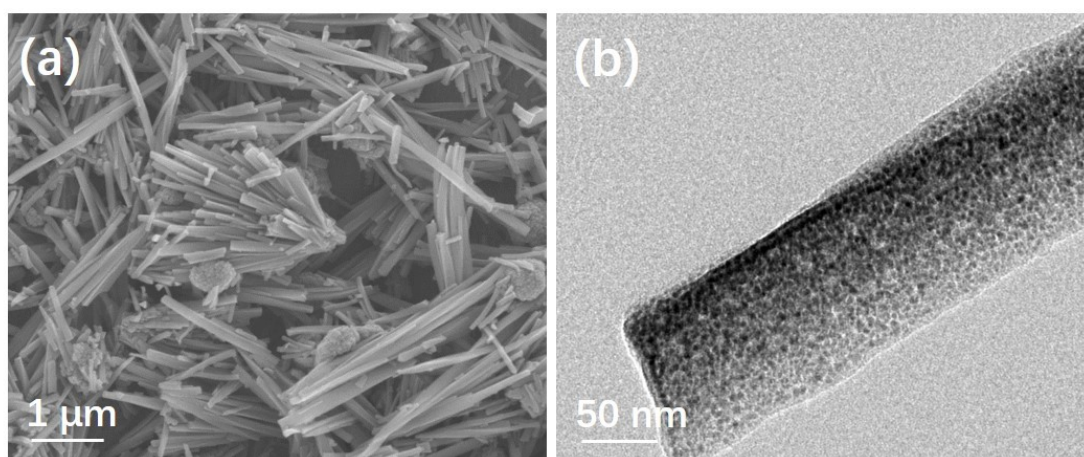


Figure S4. (a) SEM and (b) TEM images of MnO@C.

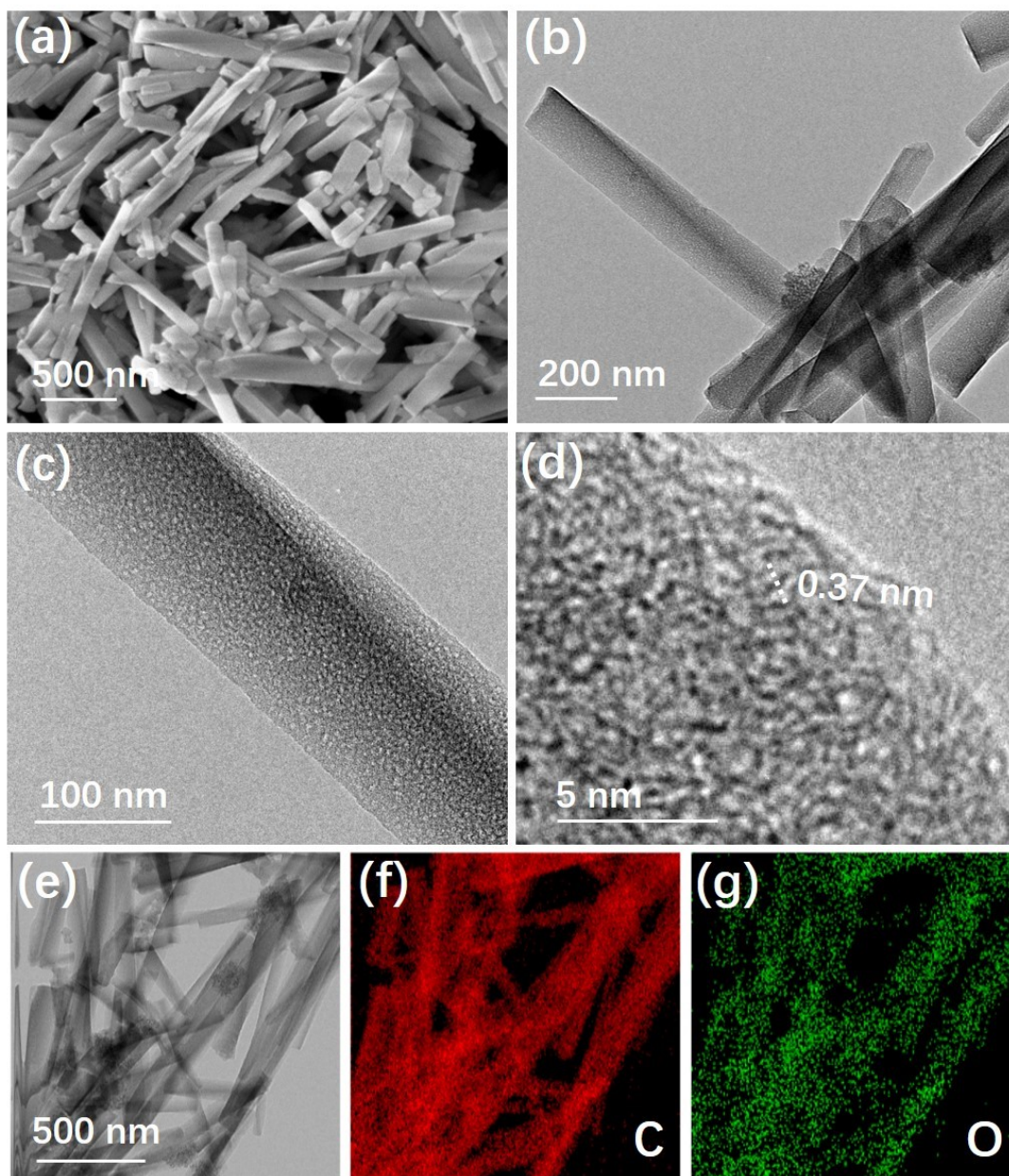


Figure S5. (a) SEM image, (b) TEM images, (c,d) HRTEM image, and (e-g) Elemental mapping images of CNTs.

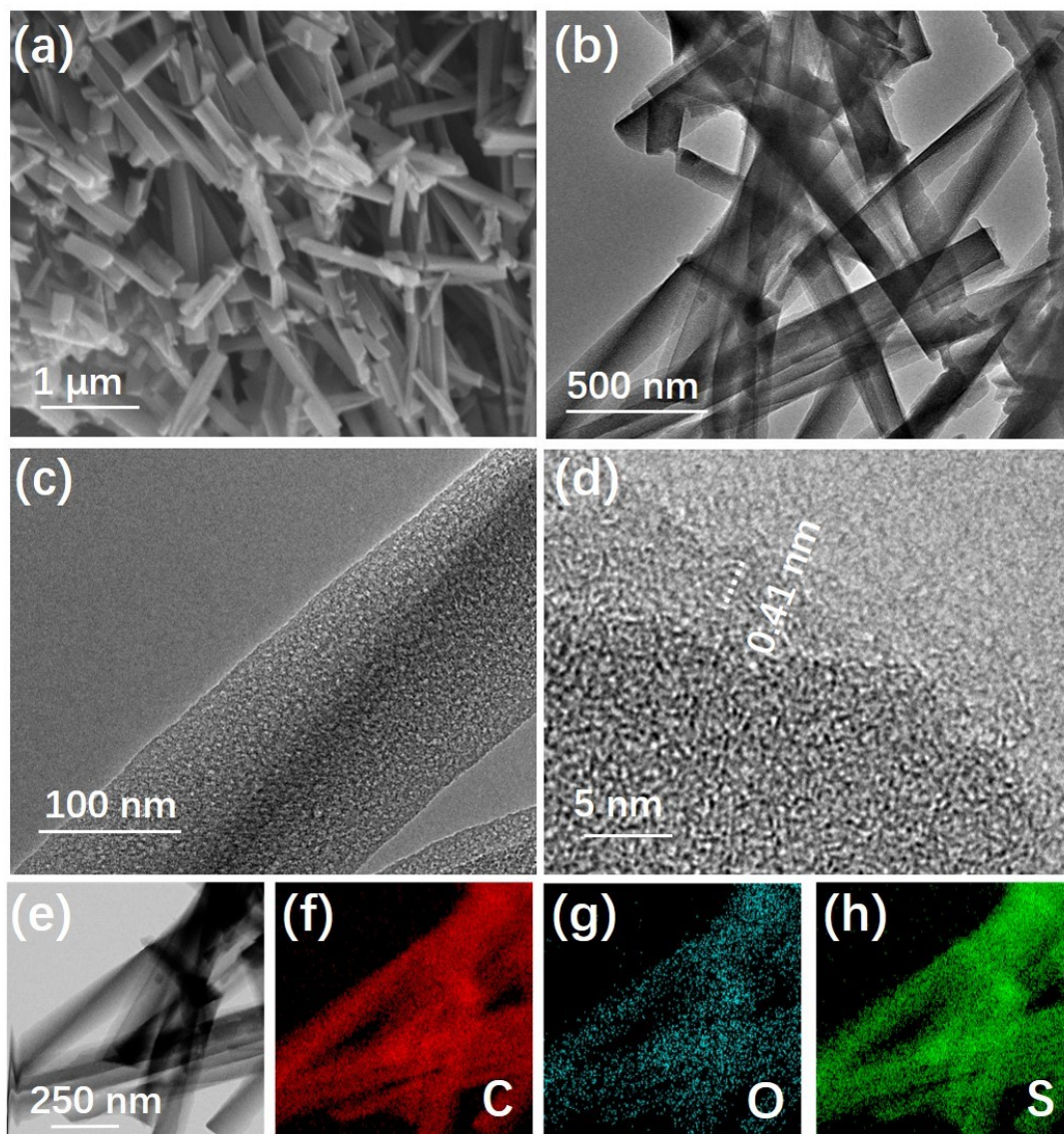


Figure S6. (a) SEM image, (b) TEM images, (c,d) HRTEM image, and (e-h) Elemental mapping images of S-CMs.

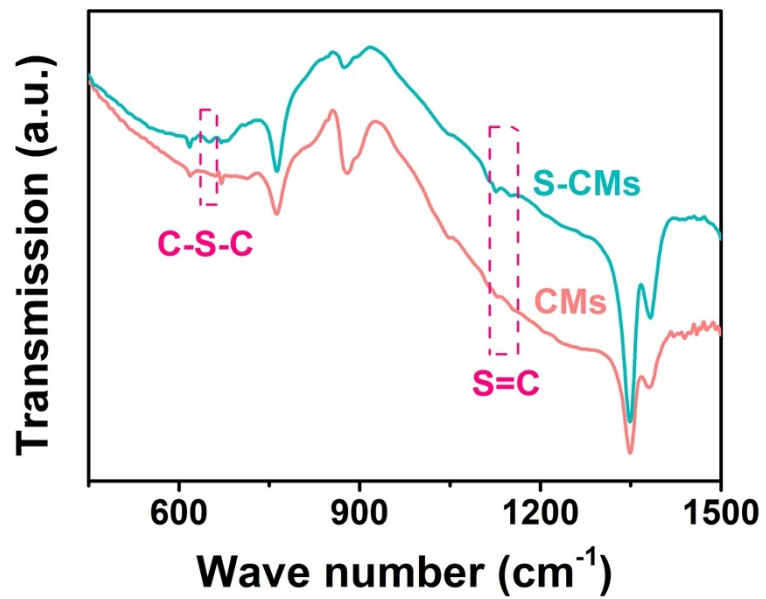


Figure S7. The FTIR spectra of S-CMs and CMs.

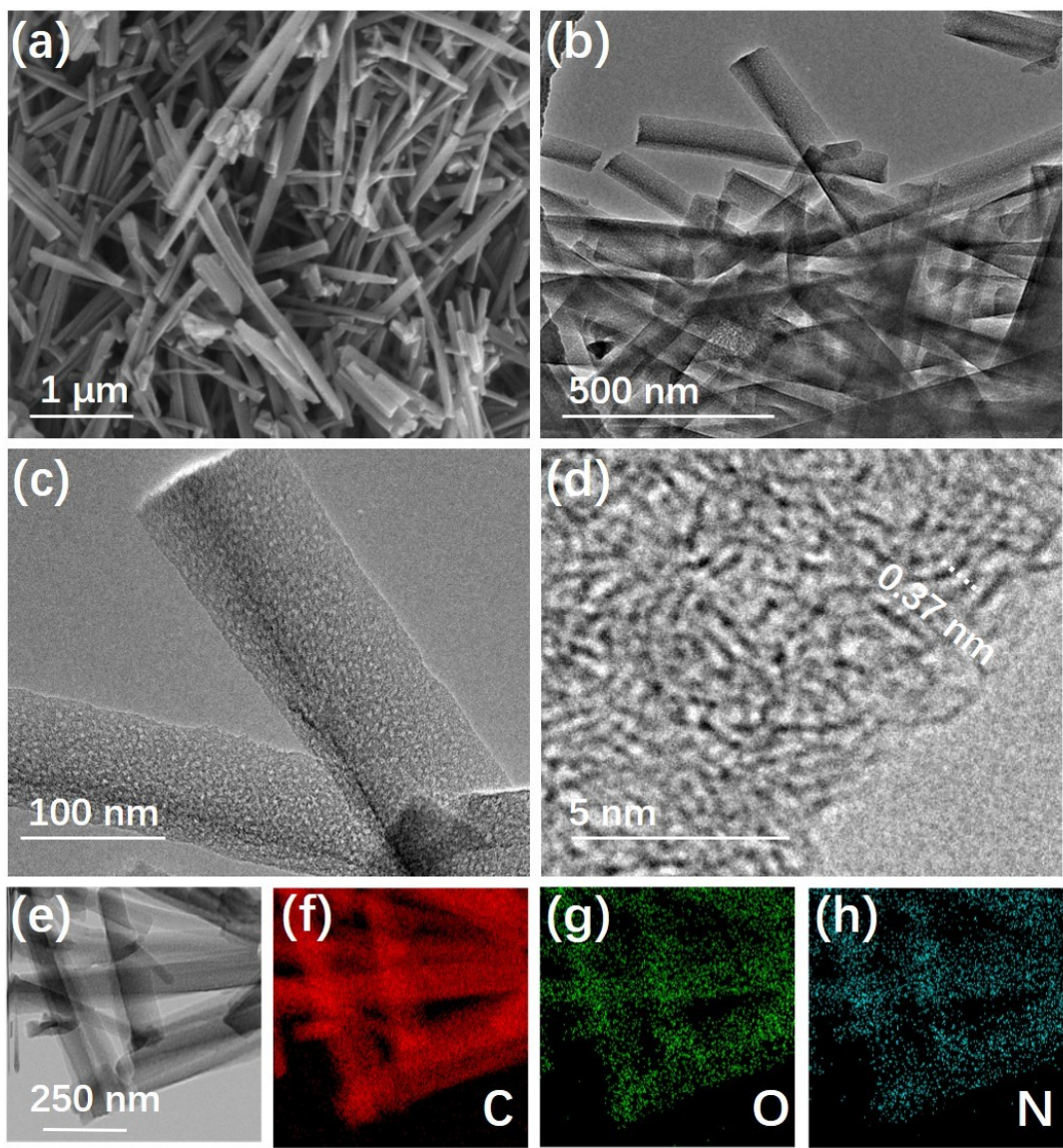


Figure S8. (a) SEM image, (b) TEM images, (c,d) HRTEM image, and (e-h) Elemental mapping images of N-CMs.

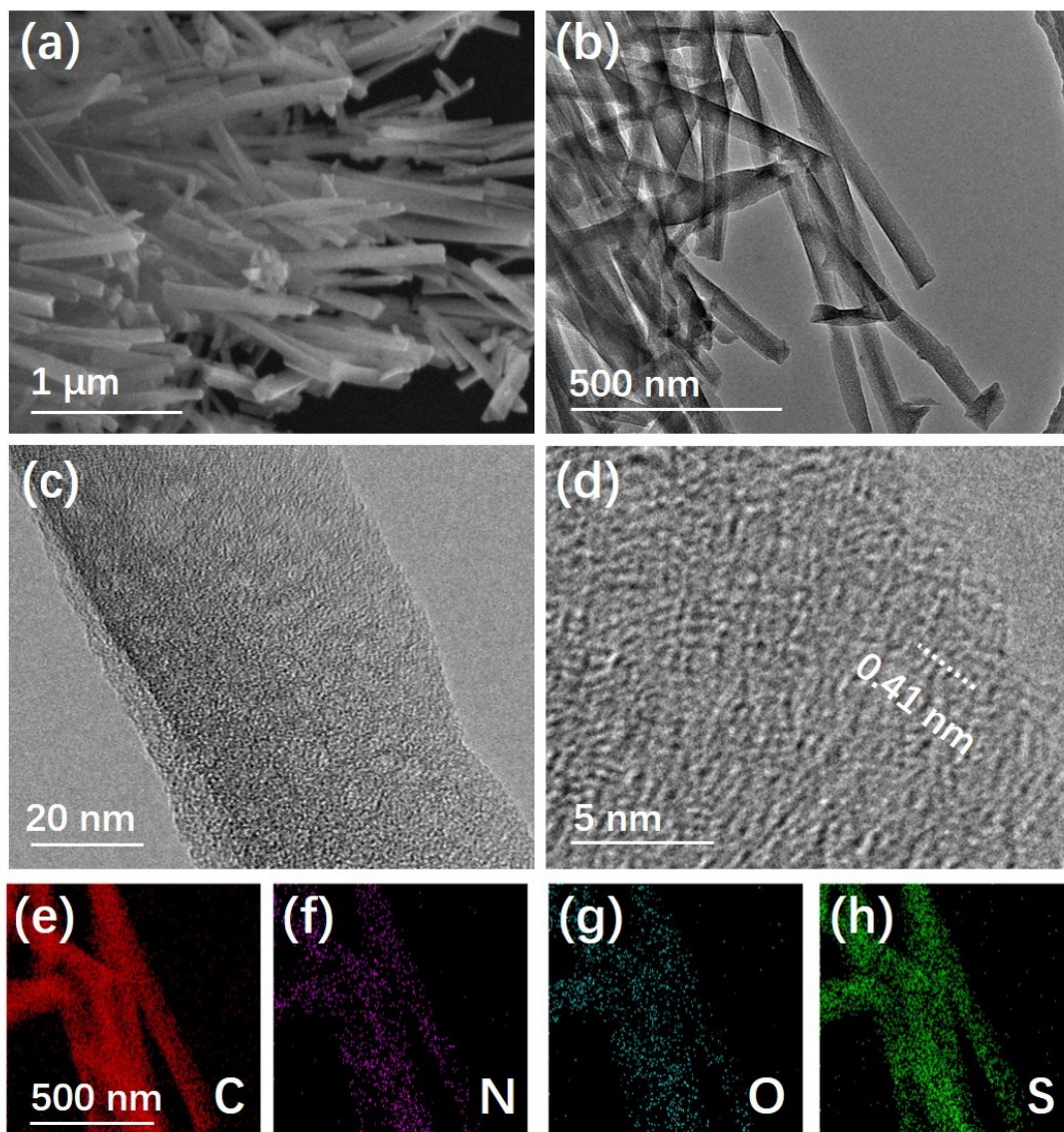


Figure S9. (a) SEM image, (b) TEM images, (c,d) HRTEM image, and (e-h) Elemental mapping images of N/S-CMs.

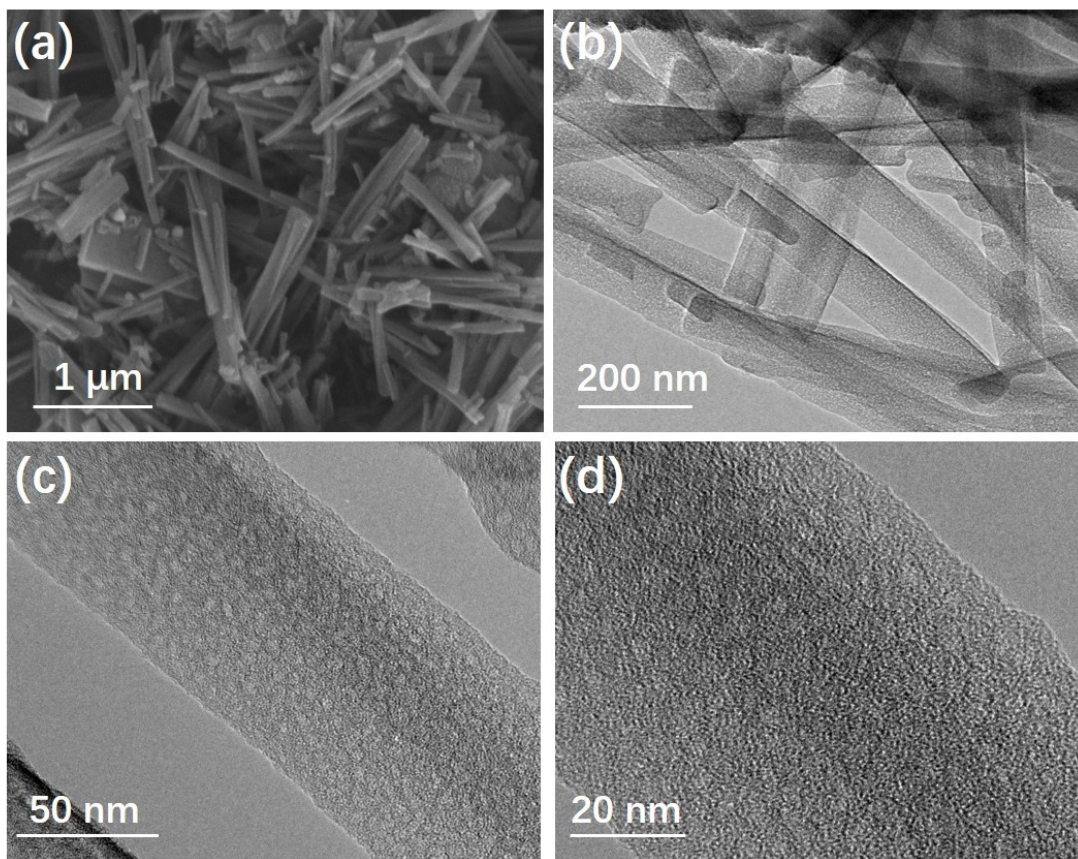


Figure S10. (a) SEM image, (b) TEM image, and (c,d) HRTEM images of S/N-CMs-700.

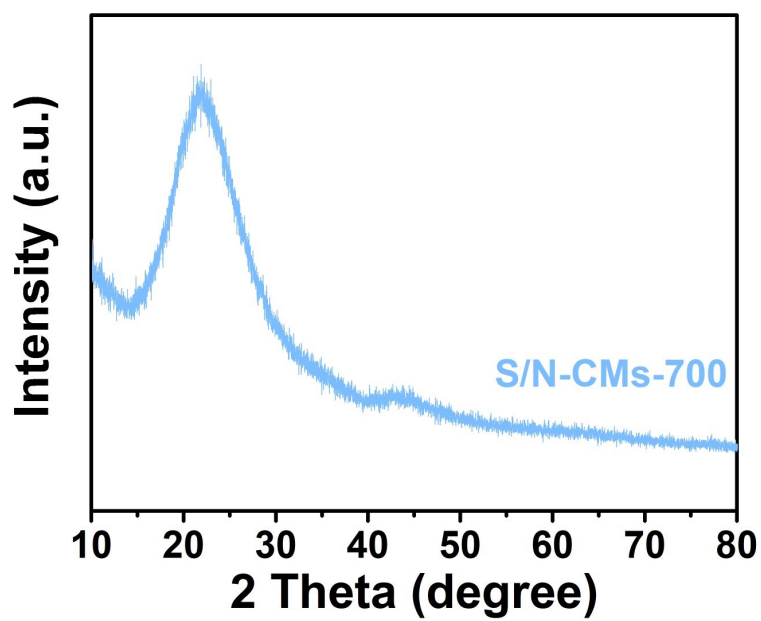


Figure S11. The XRD pattern of S/N-CMs-700.

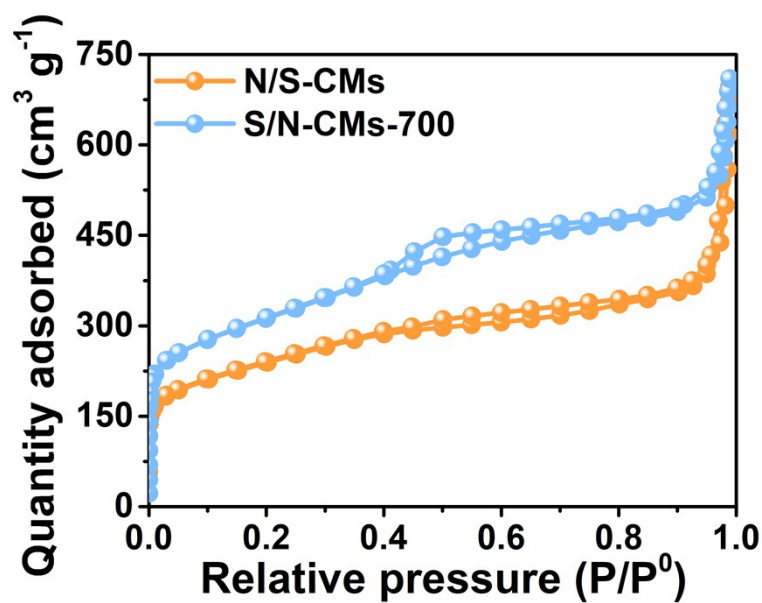


Figure S12. The N_2 adsorption/desorption isotherms of N/S-CMs-600 and S/N-CMs-700.

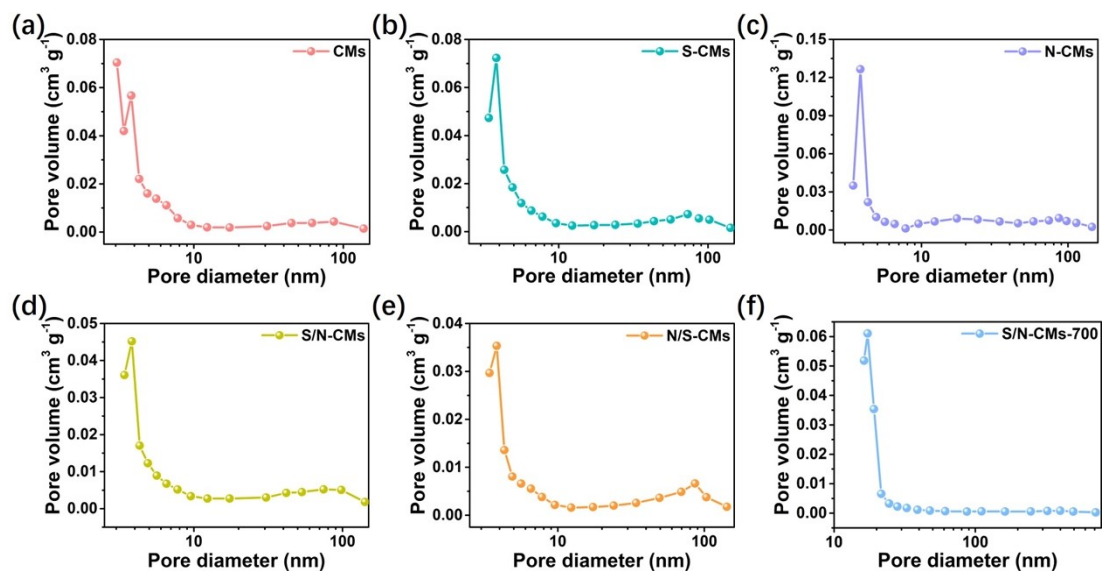


Figure S13. The pore size distribution curves of (a) CMs, (b) S -CMs, (c) N-CMs, (d) S/N-CMs, (e) N/S-CMs, and (f) S/N-CMs-700.

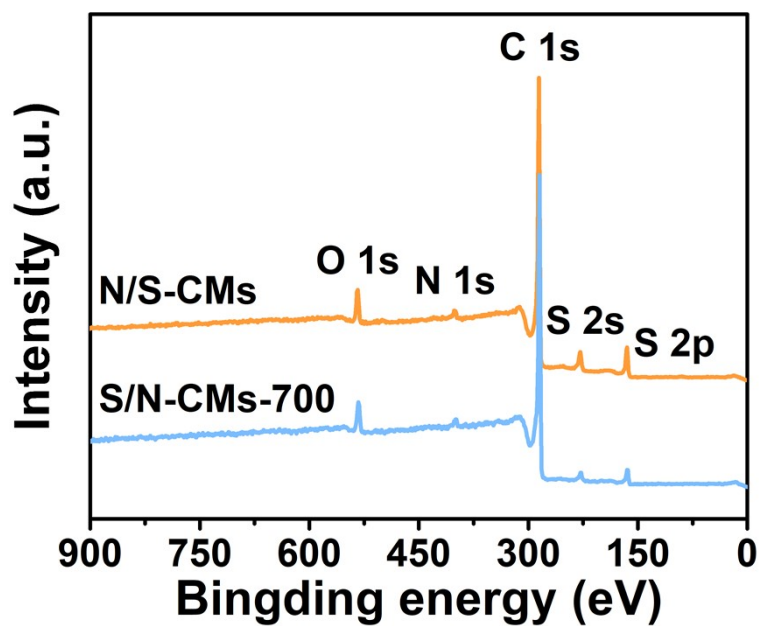


Figure S14. The full spectra of N/S-CMs and S/N-CMs-700.

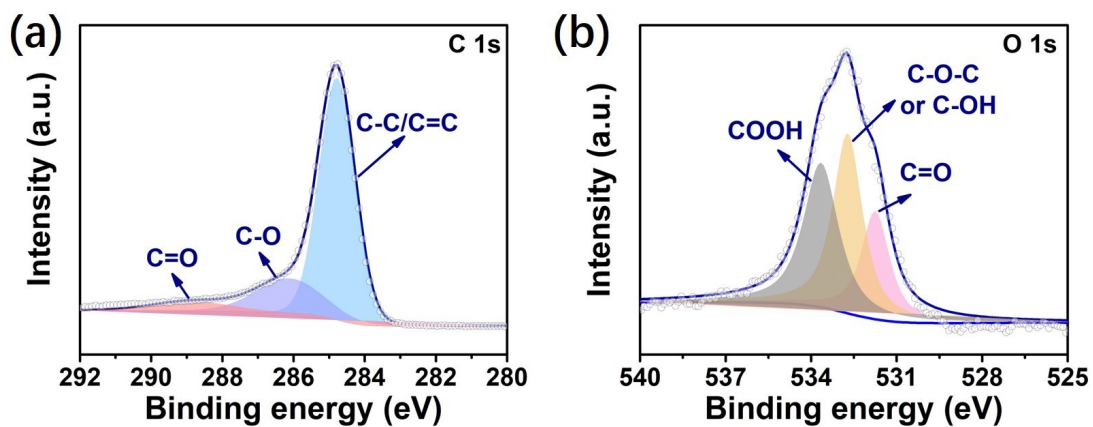


Figure S15. The high-resolution XPS spectra for (a) C 1s and (b) O 1s of CMs.

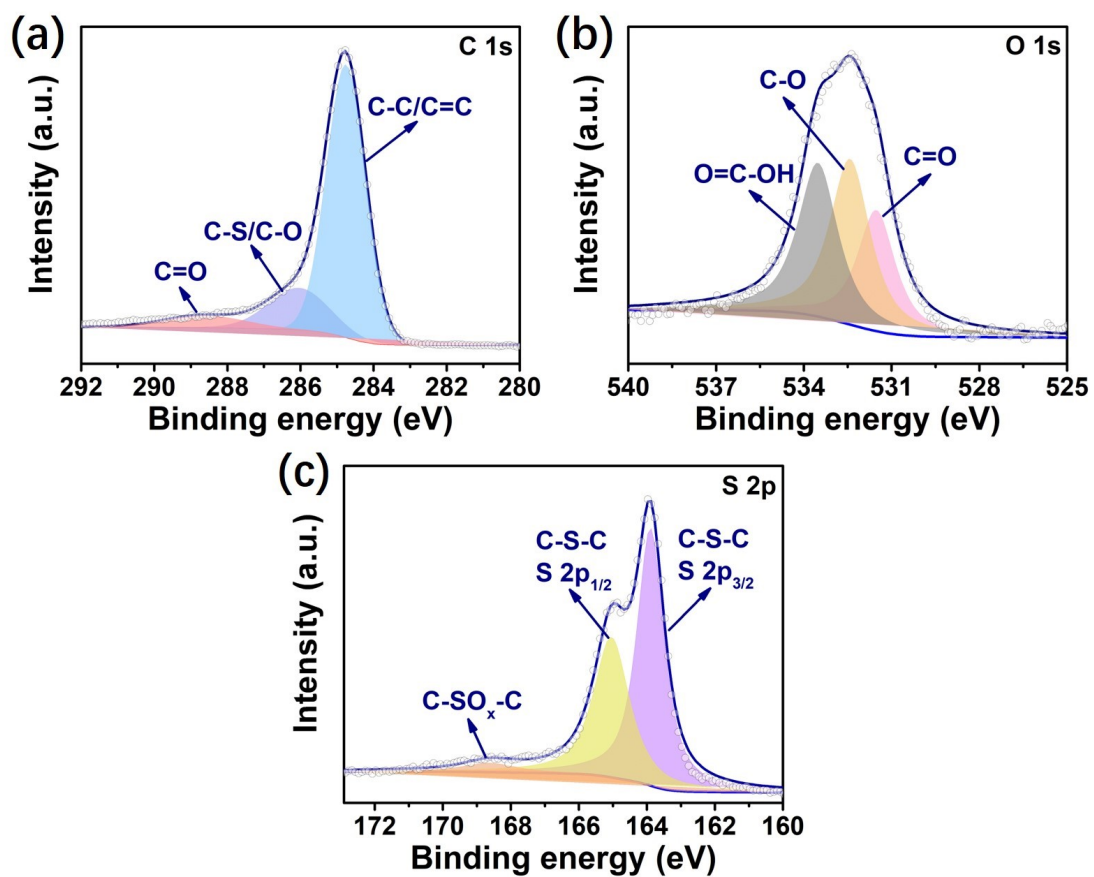


Figure S16. The high-resolution XPS spectra for (a) C 1s, (b) O 1s and (c) S 2p of S-CMs.

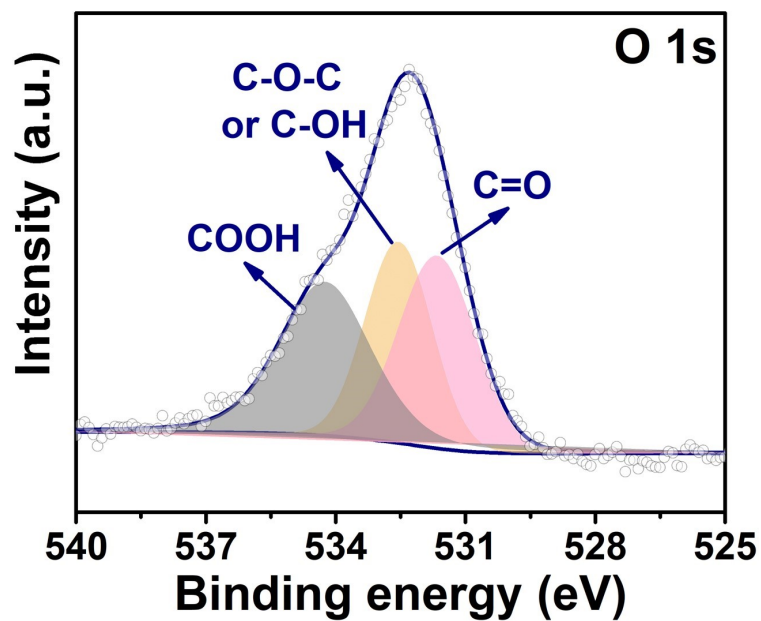


Figure S17. The high-resolution XPS spectrum for O 1s of S/N-CMs.

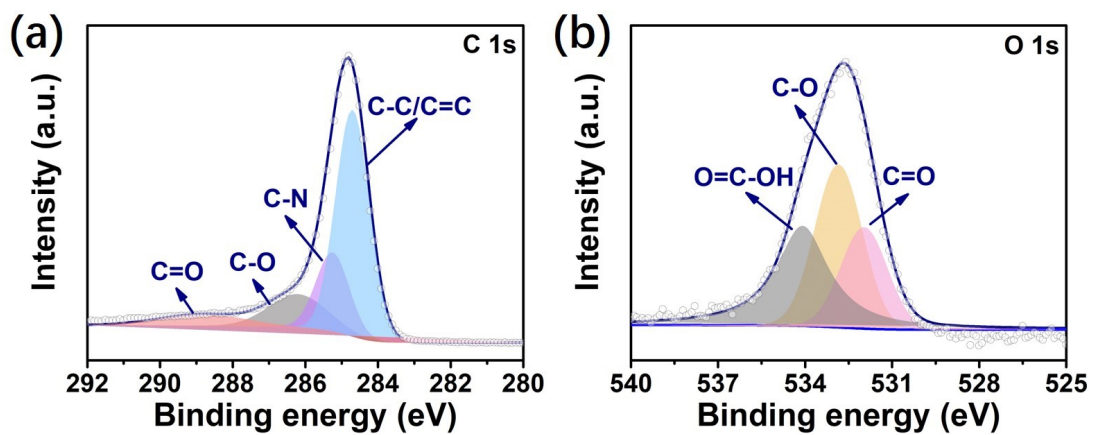


Figure S18. The high-resolution XPS spectra for (a) C 1s and (b) O 1s of N-CMs.

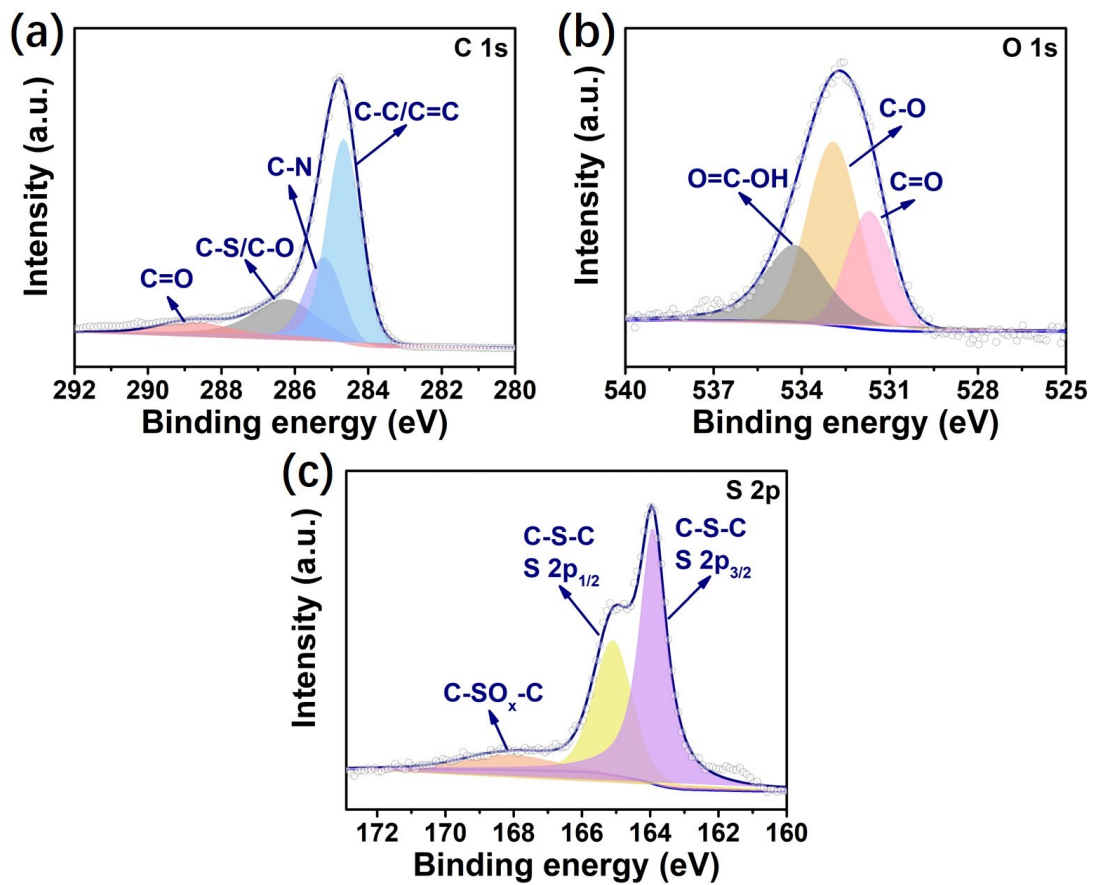


Figure S19. The high-resolution XPS spectra for (a) C 1s, (b) O 1s and (c) S 2p of N/S-CMs.

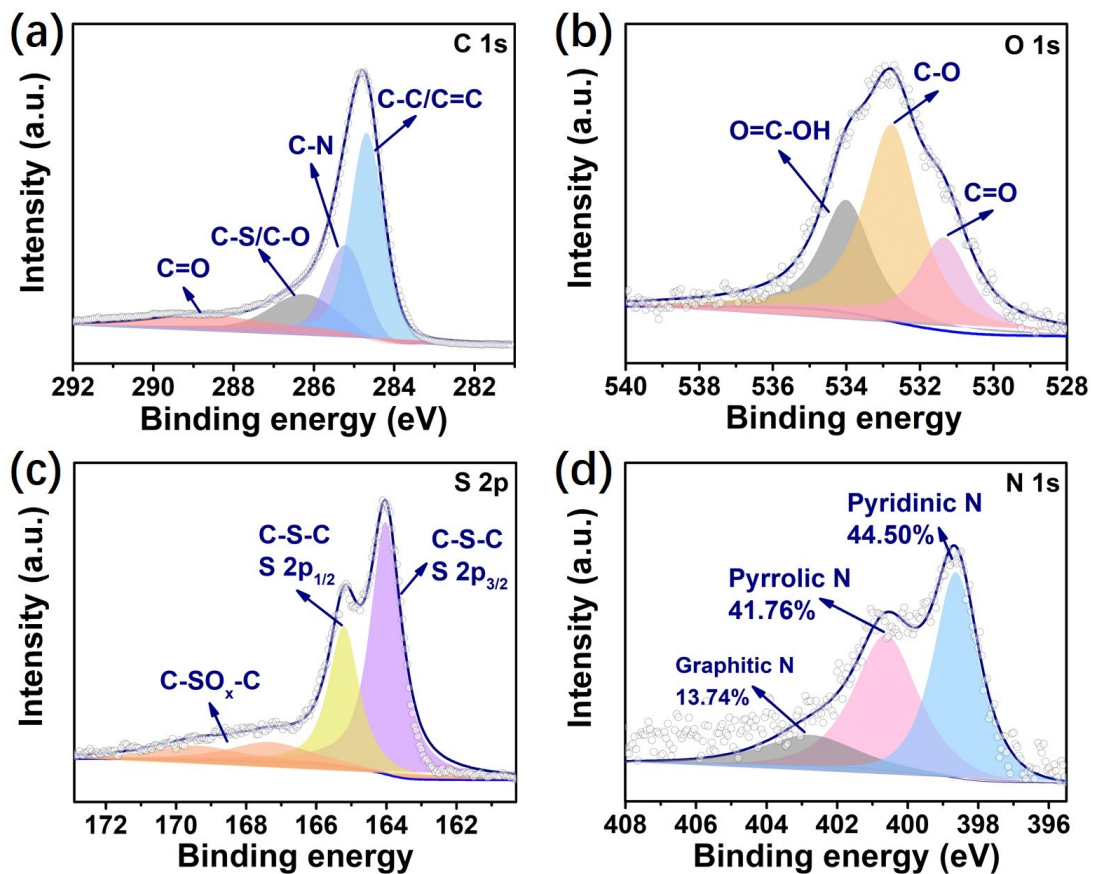


Figure S20. The high-resolution XPS spectra for (a) C 1s, (b) O 1s (c) S 2p and (d) N

1s of S/N-CMs-700.

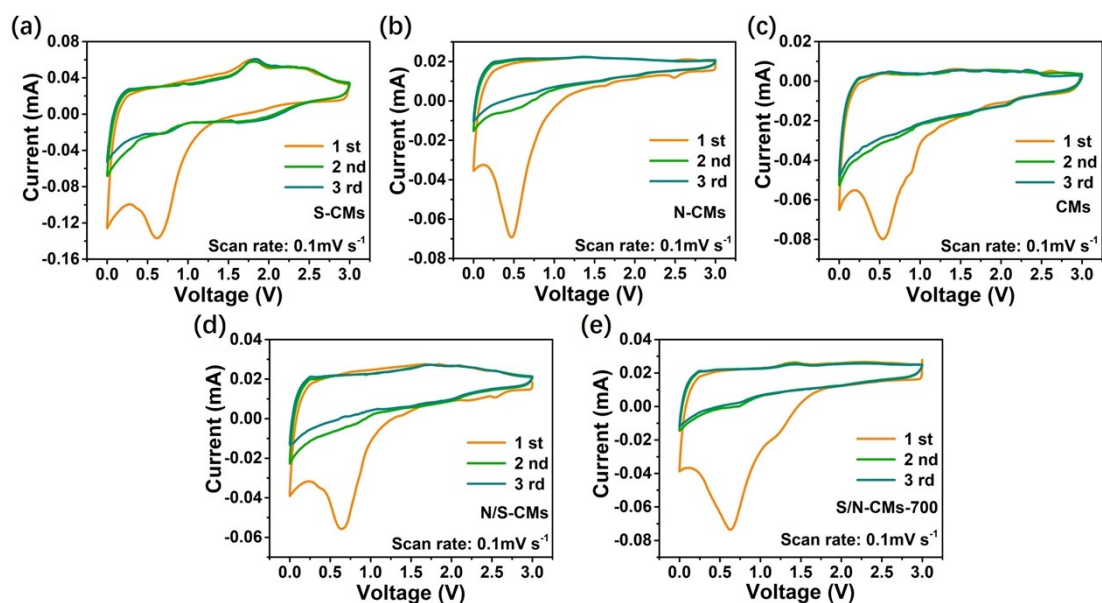


Figure S21. CV curves of (a) S-CMs, (b) N-CMs, (c) CMs, (d) N/S-CMs, and (e) S/N-CMs-700 at 0.1 mV s^{-1} .

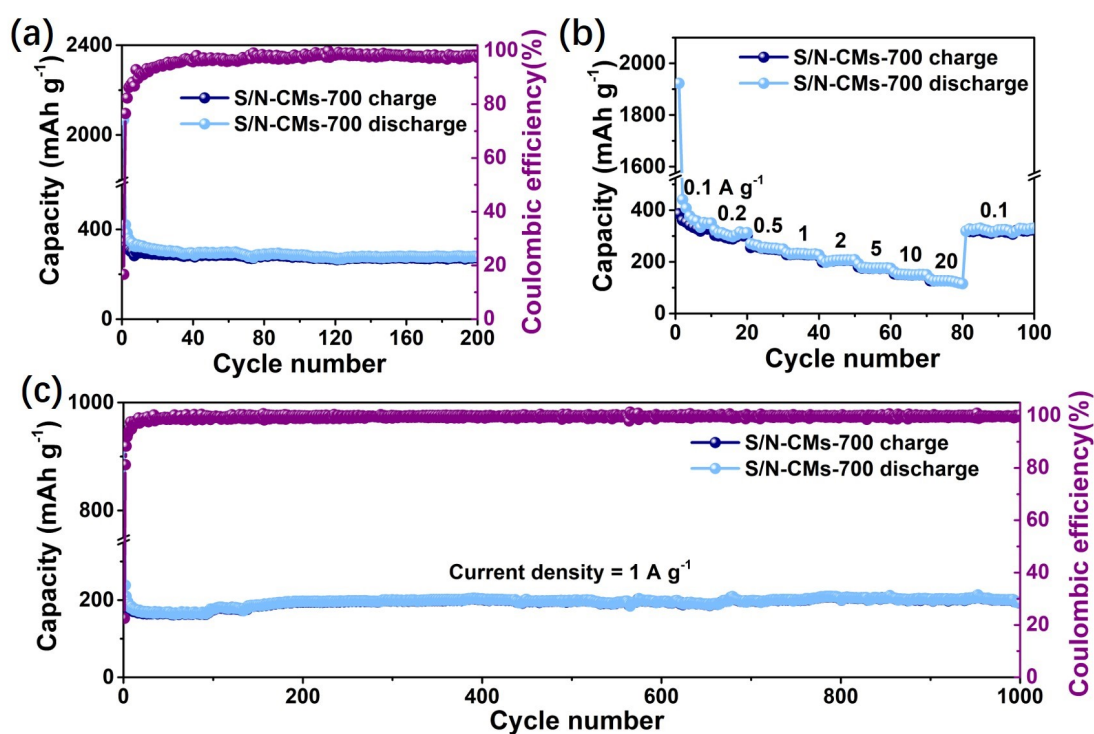


Figure S22. (a) The cycling performance of S/N-CMs-700 at 100 mA g^{-1} . (b) The rate capability of S/N-CMs-700 at a current density from 0.1 to 20 A g^{-1} . (c) The cycling performance of S/N-CMs-700 at 1 A g^{-1} .

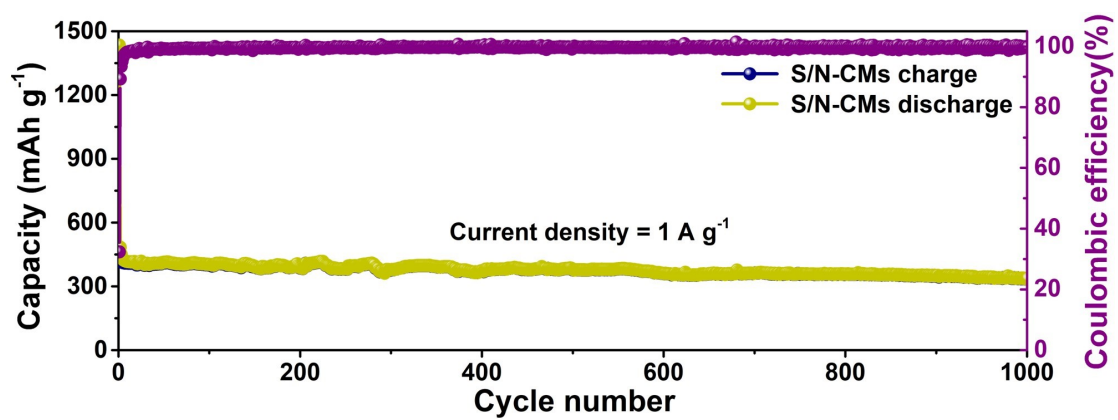


Figure S23. The cycling performance of S/N-CMs at 1 A g⁻¹.

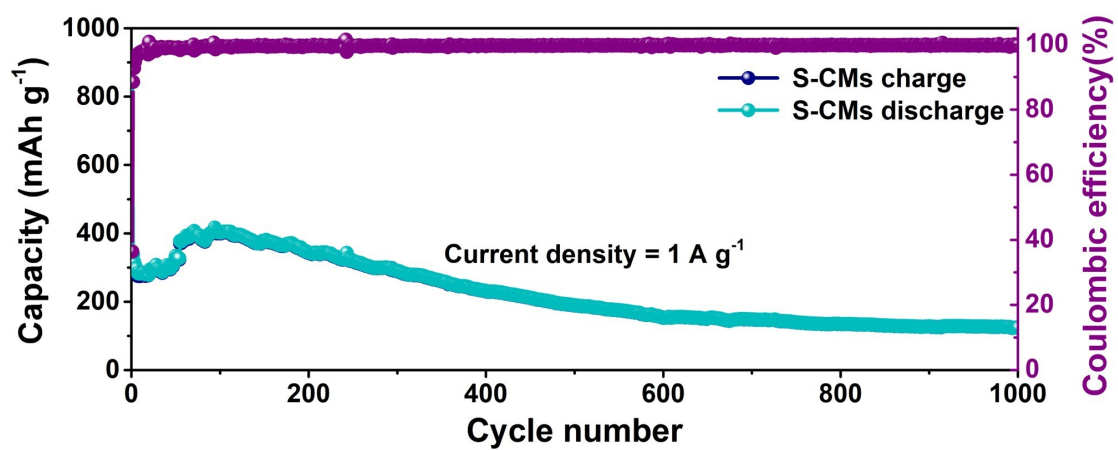


Figure S24. The cycling performance of S-CMs at 1 A g⁻¹.

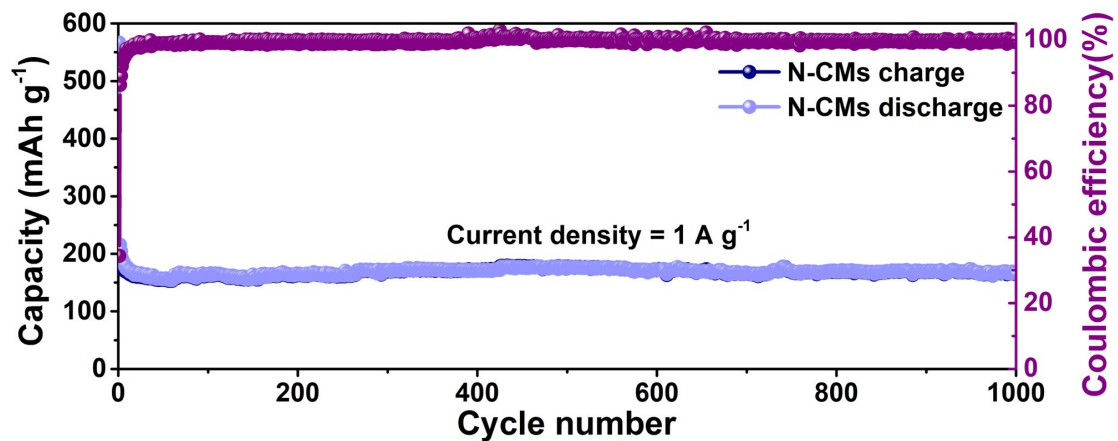


Figure S25. The cycling performance of N-CMs at 1 A g^{-1} .

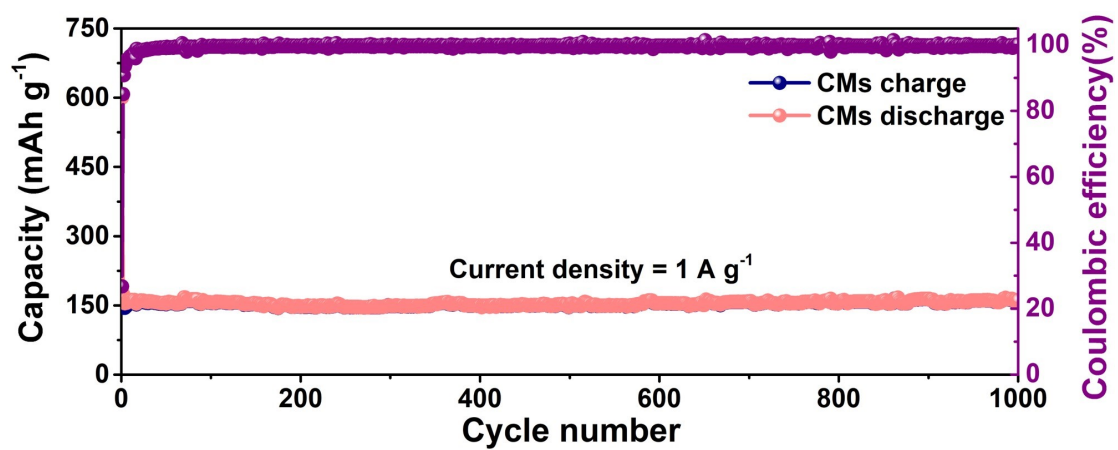


Figure S26. The cycling performance of CMs at 1 A g^{-1} .

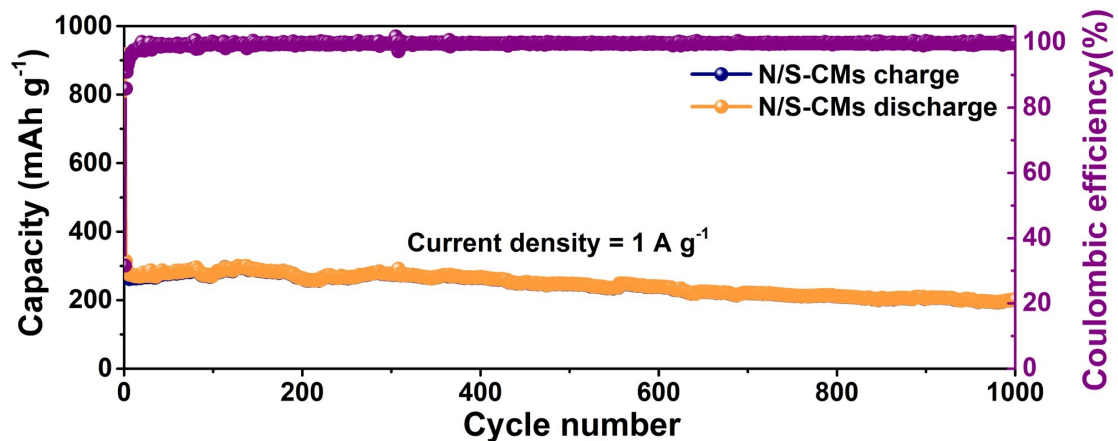


Figure S27. The cycling performance of N/S-CMs at 1 A g^{-1} .

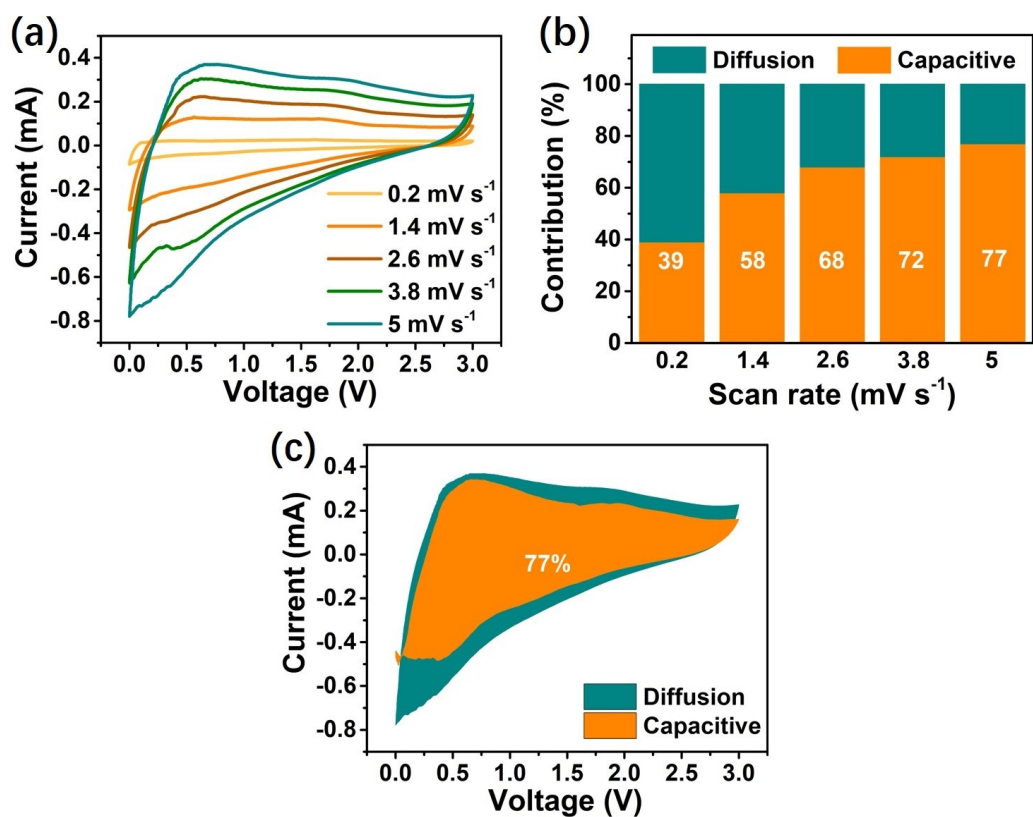


Figure S28. (a) CV curves of CMs at different scan rates. (b) Capacitive charge-storage contribution ratios in CMs at different scan rates of 0.2 to 5.0 mV s⁻¹. (c) Contribution ratio of the capacitive process in CMs at a scan rate of 5.0 mV s⁻¹.

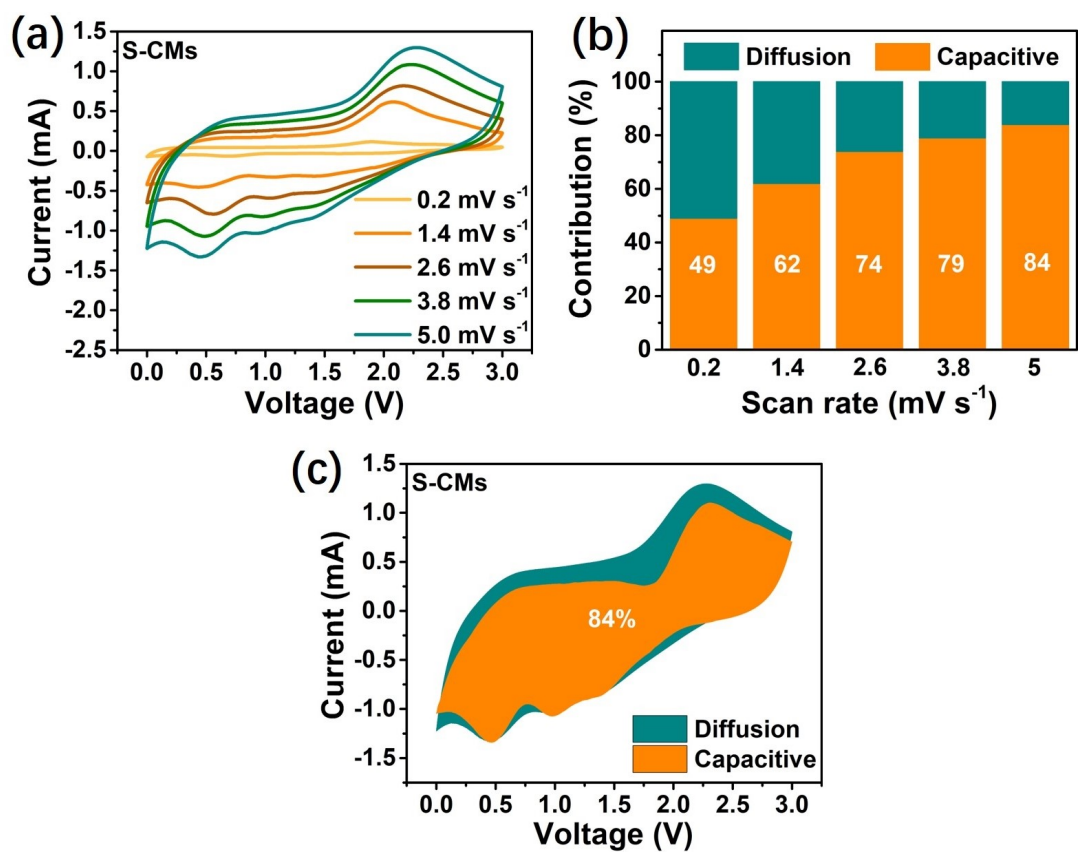


Figure S29. (a) CV curves of S-CMs at different scan rates. (b) Capacitive charge-storage contribution ratios in S-CMs at different scan rates of 0.2 to 5.0 mV s^{-1} . (c) Contribution ratio of the capacitive process in S-CMs at a scan rate of 5.0 mV s^{-1} .

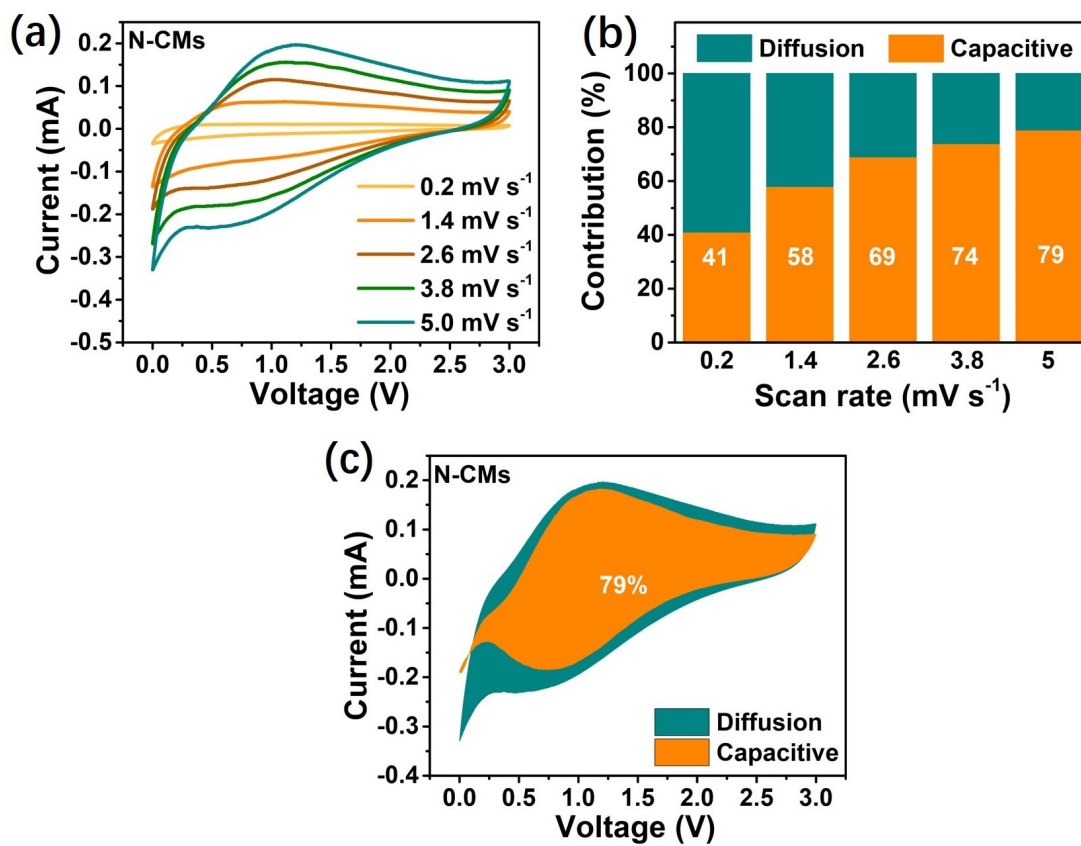


Figure S30. (a) CV curves of N-CMs at different scan rates. (b) Capacitive charge-storage contribution ratios in N-CMs at different scan rates of 0.2 to 5.0 mV s^{-1} . (c) Contribution ratio of the capacitive process in N-CMs at a scan rate of 5.0 mV s^{-1} .

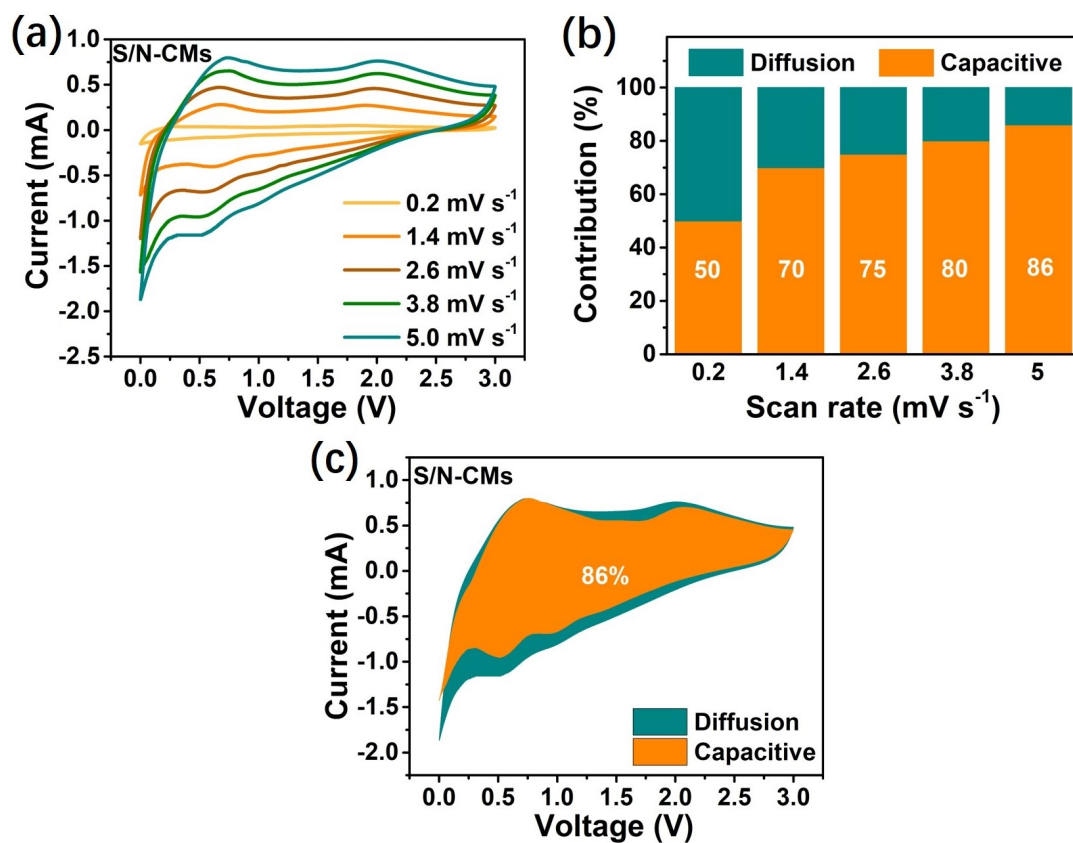


Figure S31. (a) CV curves of S/N-CMs at different scan rates. (b) Capacitive charge-storage contribution ratios in S/N-CMs at different scan rates of 0.2 to 5.0 mV s⁻¹. (c) Contribution ratio of the capacitive process in S/N-CMs at a scan rate of 5.0 mV s⁻¹.

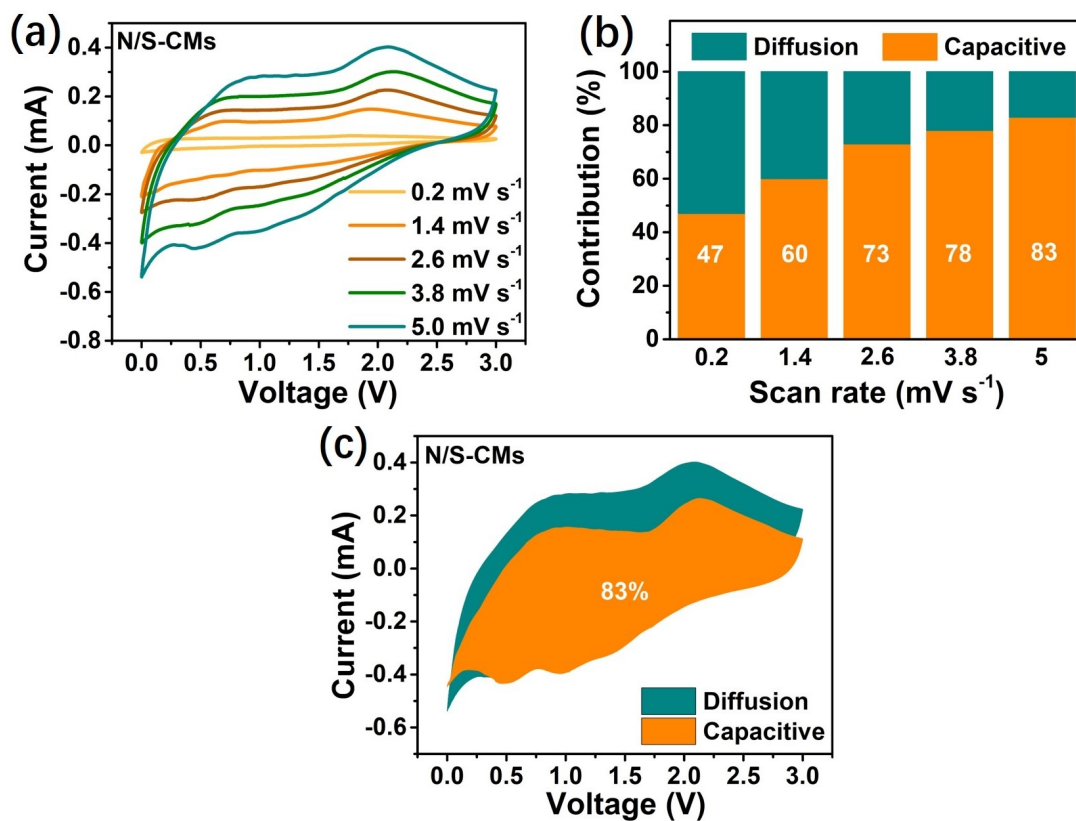


Figure S32. (a) CV curves of N/S-CMs at different scan rates. (b) Capacitive charge-storage contribution ratios in N/S-CMs at different scan rates of 0.2 to 5.0 mV s^{-1} . (c) Contribution ratio of the capacitive process in N/S-CMs at a scan rate of 5.0 mV s^{-1} .

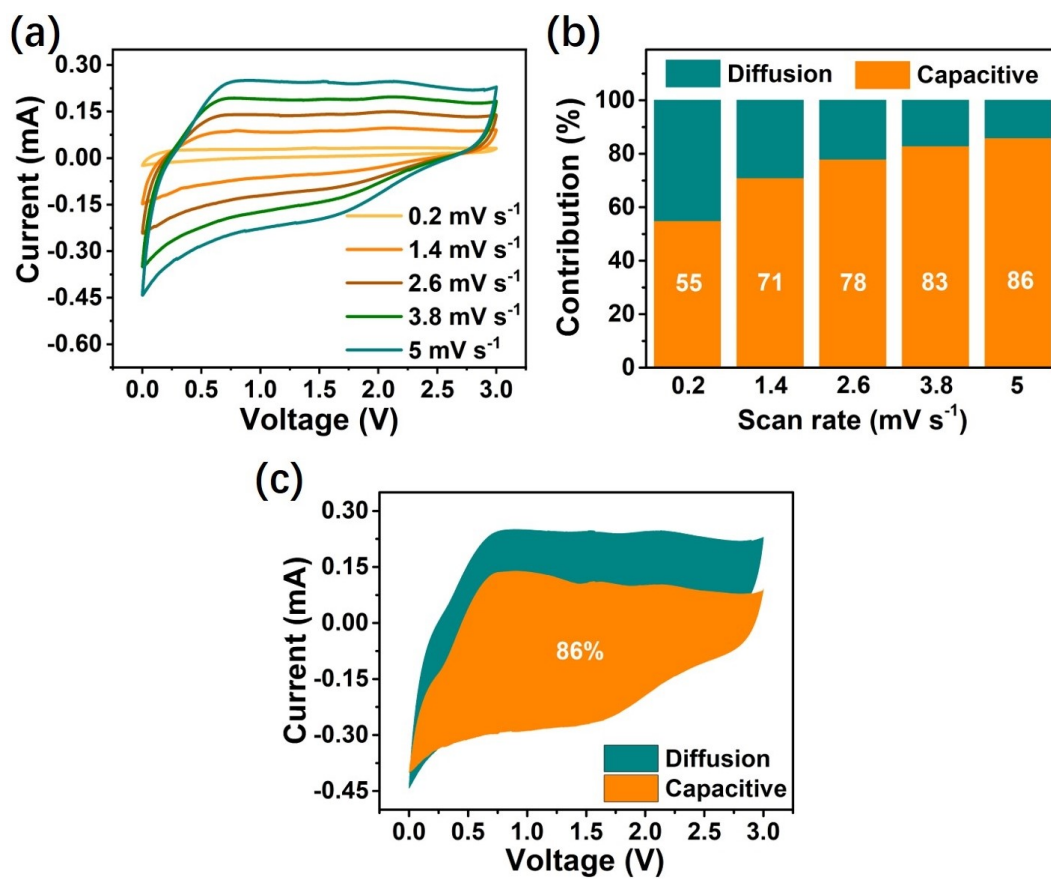


Figure S33. (a) CV curves of S/N-CMs-700 at different scan rates. (b) Capacitive charge-storage contribution ratios in S/N-CMs-700 at different scan rates of 0.2 to 5.0 mV s⁻¹. (c) Contribution ratio of the capacitive process in S/N-CMs-700 at a scan rate of 5.0 mV s⁻¹.

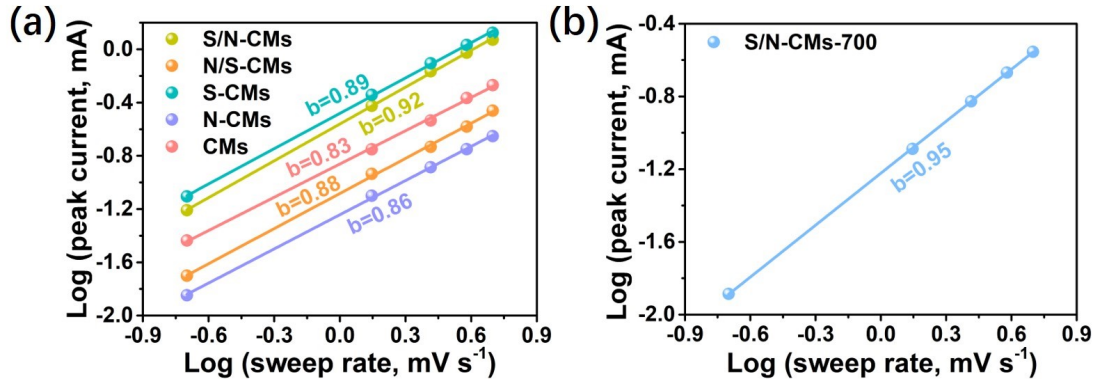


Figure S34. The b values of (a) S/N-CMs, N/S-CMs, S-CMs, N-CMs and CMs, and (b) S/N-CMs-700.

Besides, the current peak (i) and scan rate (v) are correlated with a power law relationship: ^[S1]

$$i = av^b \quad (1)$$

where a and b are adjustable constants. b value of 0.5 represents an ideal diffusion dominated process, while the b value of 1.0 indicates a capacitive controlled process.

In addition, the capacitive contribution for the total potassium storage capacity can be confirmed by the following equation: ^[S2]

$$i(V) = k_1v + k_2v^{1/2} \quad (2)$$

where k_1v represents the surface induced capacitive contribution and $k_2v^{1/2}$ stands for the diffusion-controlled contribution.

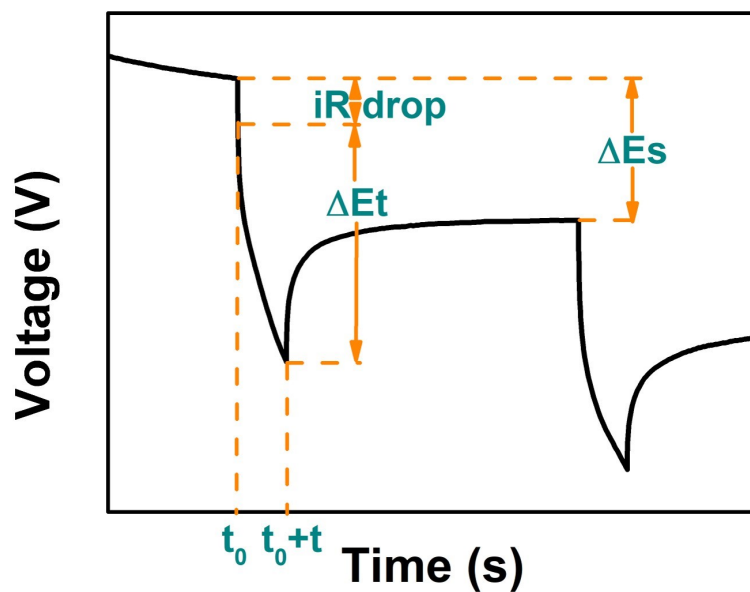


Figure S35. Schematic of the calculation of diffusion coefficient using the GITT technique.

The diffusion coefficient is calculated according to the equation:^[S3]

$$D = \frac{4}{\pi\tau} \left[\frac{m_B V_M}{M_B S} \right]^2 \left[\frac{\Delta E_s}{\Delta E_\tau} \right]^2$$

Where τ is the current pulse time (s), m_B , M_B , and V_M are the mass, the molar mass and the molar volume of the active material, respectively. S is the geometric area of the electrode.

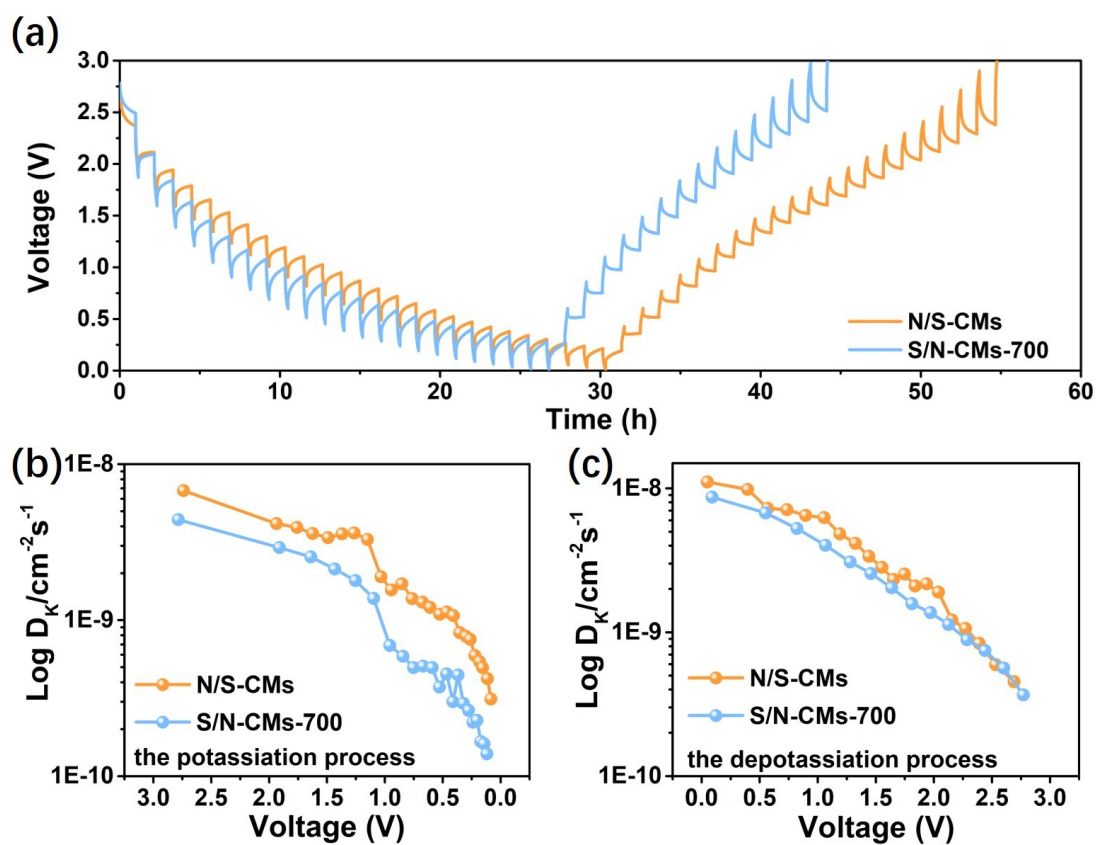


Figure S36. Kinetics analysis and potassium-storage mechanism. (a) GITT profiles of the state of the potassiation/depotassiation process. The K^+ diffusion coefficient as a function of the state of the (b) potassiation and (c) depotassiation process of N/S-CMs and S/N-CMs-700.

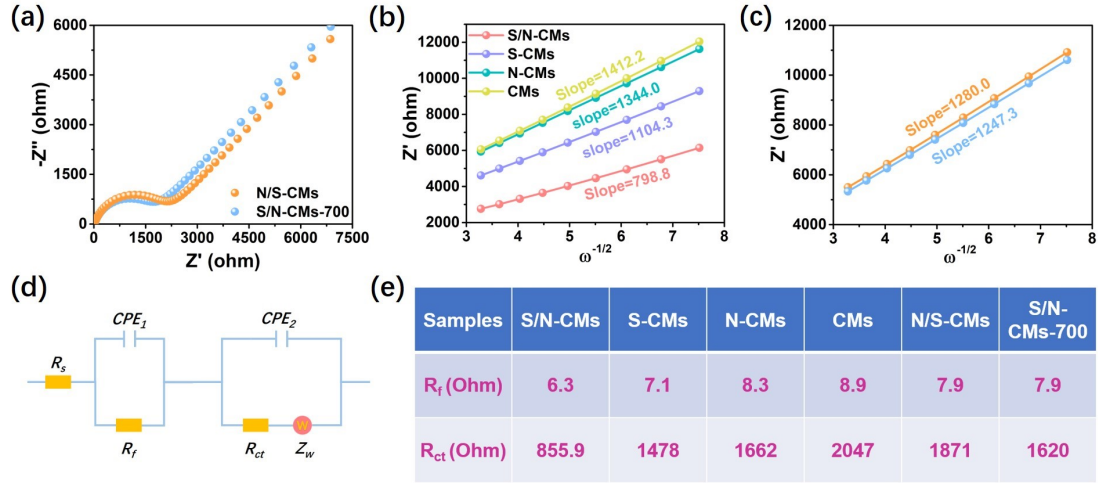


Figure S37. EIS curves. (a) Nyquist plots of N/S-CMs and S/N-CMs-700, (b) and (c) linear fits of the Z' versus $\omega^{-1/2}$ ($\omega=2\pi f$) in the low-frequency region, (d) the corresponding equivalent circuit model, (e) the EIS fitting parameters.

As shown in Fig 4d,e and S37a, the Nyquist plot mainly consists of a single depressed semicircle at high frequency region and an inclined line at low frequency region. The EIS spectrum can be fit with an equivalent circuit modeled, where R_s , R_{ct} , and R_f represent the total ohmic resistance of the electrode system, the charge transfer resistance in the middle-frequency region, and the SEI membrane resistance in the high-frequency region, respectively. Z_w is the Warburg impedance for K^+ diffusion in most electrode materials in relation to the straight slope in the low frequency region. CPE-1 and CPE-2 are related to surface capacitance and double layer capacitance, respectively.^[S4,S5]

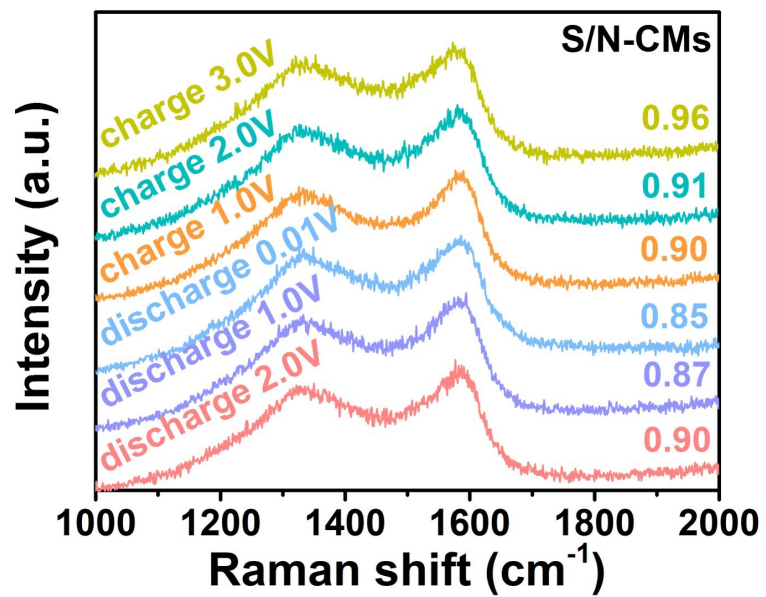


Figure S38. Ex-situ Raman of S/N-CMs.

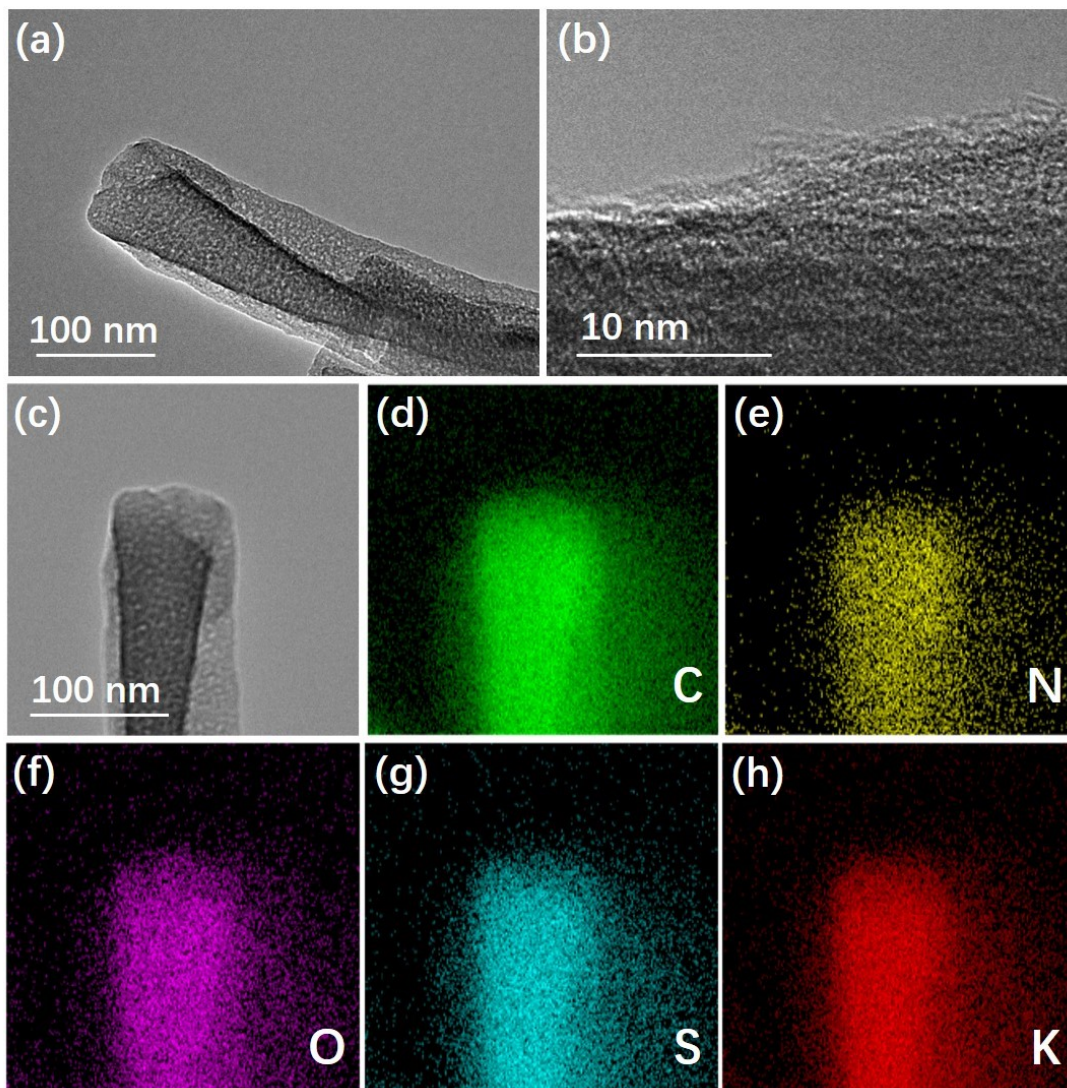


Figure S39. (a,b) The *Ex-situ* HRTEM images and (c-h) EDS mapping images of S/N-CMs.

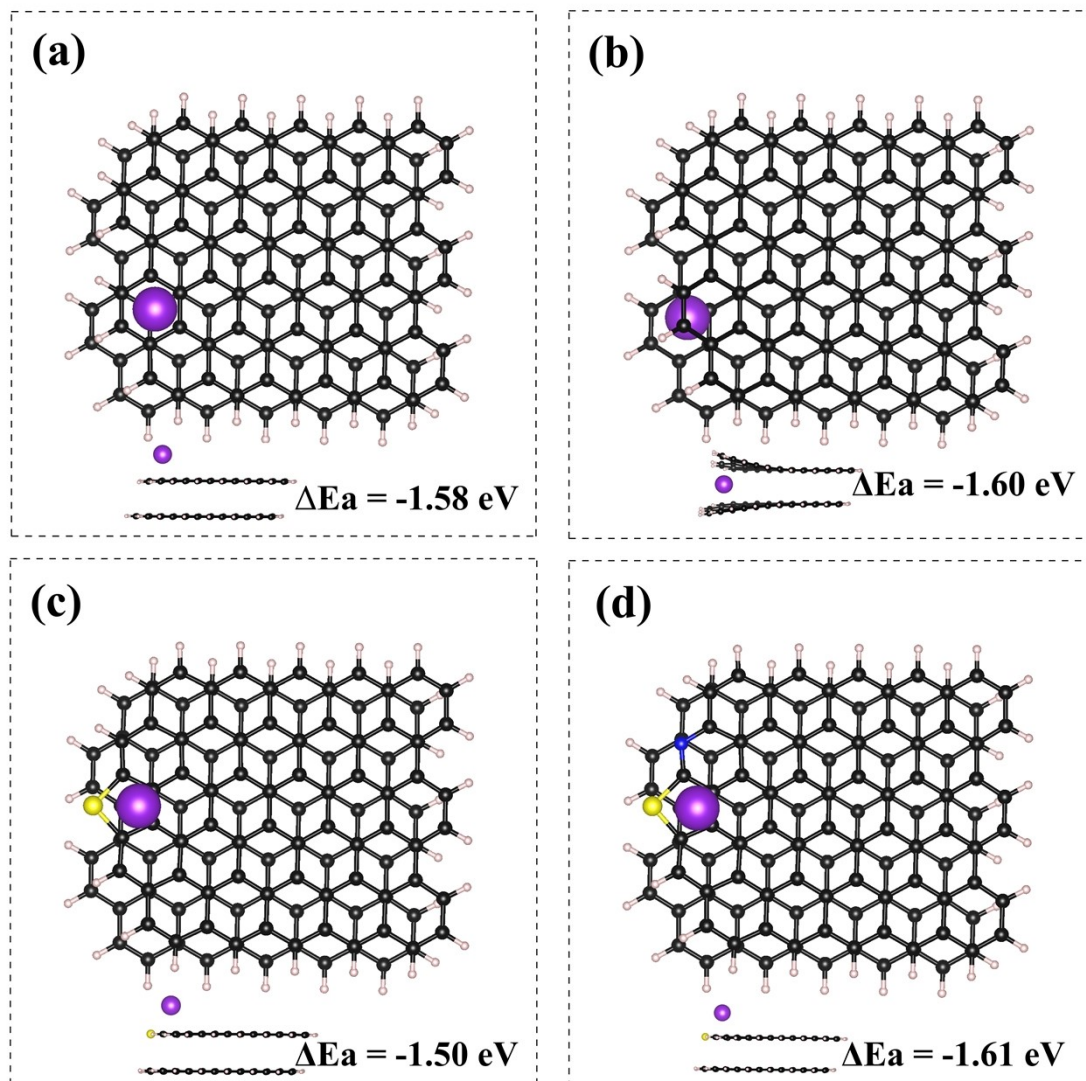


Figure S40. The pristine graphene model adsorption energy for K both out of (a) interlayer (-1.58 eV) and (b) within interlayer (-1.60 eV). The interlayer adsorption energy for K of (c) pure S doped graphene model (-1.50 eV) and (d) S, N co-doped graphene model (-1.61 eV).

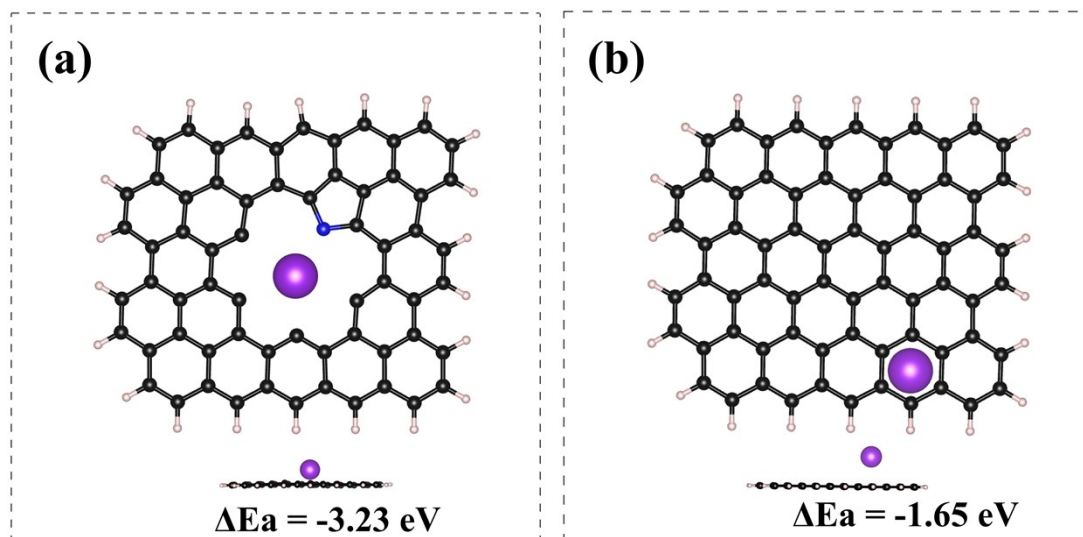


Figure S41. The adsorption energy of (a) pyrrolic N (-3.23 eV) and (b) pristine graphene (-1.65 eV) for K.

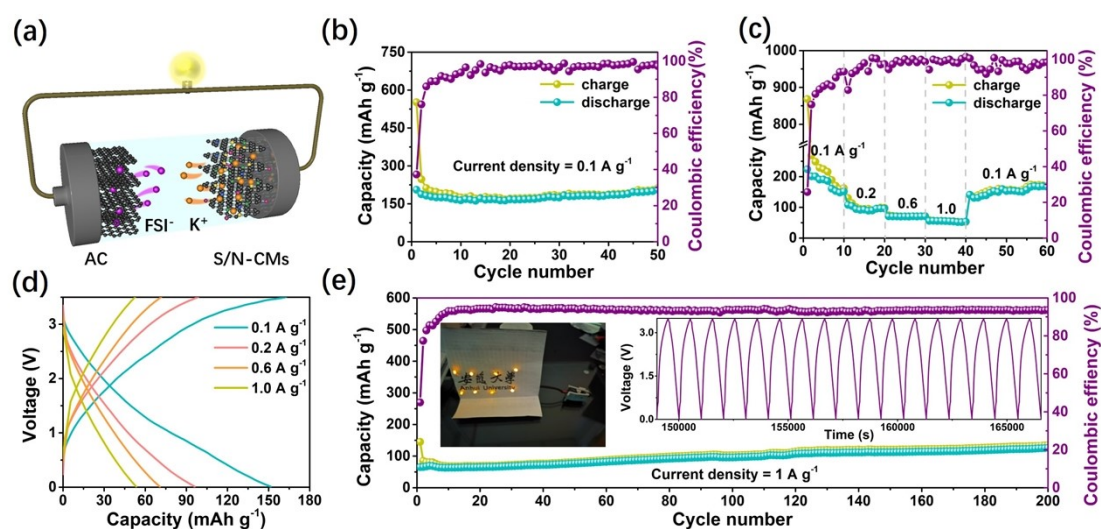


Figure S42. Electrochemical performance of S/N-CMs||AC PIHCs. (a) Schematic illustration, (b) Cycling stability at the current density of 0.1 A g^{-1} , (c) Rate capability, (d) GCD curves at different current densities, (e) Long-term cycling stability at the current density of 1 A g^{-1} and the inset is a LED light.

Table S1. The N₂ adsorption/desorption isotherms results of all electrode materials.

Samples	Specific surface area (m ² g ⁻¹)	Pore volume (cm ³ g ⁻¹)	Pore diameter (nm)
CMs	808.7	0.532	4.350
N-CMs	1006.4	1.008	5.794
S-CMs	765.9	0.688	4.729
S/N-CMs	905.2	0.625	4.623
N/S-CMs	840.1	0.553	5.125
S/N-CMs-700	1101.2	0.644	19.942

Table S2. The elements content of all electrode materials.

Samples	Element composition from XPS (%)								
	S(at%)	N(at%)	N-6	N-5	N-Q	O(at%)	C=O	C-O	-COOH
CMs						7.5	23.0	39.6	37.4
N-CMs		3.2	39.1	45.6	15.3	4	24.1	39.0	36.9
S-CMs	7.1					4.7	26.4	38.4	35.2
S/N-CMs	3.0	5.1	39.4	48.5	12.1	4.2	33.7	30.7	35.6
N/S-CMs	4.4	2.5	30.8	53.1	16.1	3.8	26.2	46.1	27.7
S/N-CMs-700	2.5	2.8	44.5	41.8	13.7	4.3	22.7	50.7	26.6

Table S3. Comparison of electrochemical performance of S/N-CMs electrode with those previous reported carbon-based materials for PIBs at small current densities.

Samples	Current density (A g⁻¹)	Cycle number	Capacity (mAh g⁻¹)	Ref.
S/N-CMs	0.1A	200	577	Our work
NMCP@rGO	1.0A	1000	197	S6
NPCF-800	0.1A	100	327	S7
N,S-3DHPC-600	0.1A	100	321.3	S8
ENDC500	0.2A	660	305	S9
C₃N₄@NCNF-600	0.1A	400	346	S11
S/N@C	0.1A	400	200	S12
GDY-800	0.1A	180	350	S13
NOCNBs	0.2A	120	379	S14
NOC@GF	0.1A	550	319	S15

Table S4. Comparison of electrochemical performance of S/N-CMs electrode with those previous reported carbon-based materials for PIBs at high current densities.

Samples	Current density (A g⁻¹)	Cycle number	Capacity (mAh g⁻¹)	Ref.
S/N-CMs	5.0A	10000	249	Our work
NMCP@rGO	5.0A	6000	151.4	S6
NPCF-800	1.0A	2000	258.9	S7
N,S-3DHPC-600	1.0A	1000	249.5	S8
NCFs-800	10.0A	10000	124	S10
C₃N₄@NCNF-600	1.0A	3000	204	S11
S/N@C	2.0A	900	65	S12
GDY-800	1.0A	2000	165	S13
NOCNBs	1.0A	1600	277	S14
NOC@GF	1.0A	5500	281	S15

References

- [S1] M. Shao, C. Li, T. Li, H. Zhao, W. Yu, R. Wang, J. Zhang and L. Yin, *Adv. Funct. Mater.*, 2020, **30**, 2006561.
- [S2] K. Chu, X. Zhang, Y. Yang, Z. Li, L. Wei, G. Yao, F. Zheng and Q. Chen, *Carbon*, 2021, **184**, 277-286.
- [S3] X. Hu, G. Zhong, J. Li, Y. Liu, J. Yuan, J. Chen, H. Zhan and Z. Wen, *Energy Environ. Sci.*, 2020, **13**, 2431-2440.
- [S4] B. Liu, Y. Liu, X. Hu, G. Zhong, J. Li, J. Yuan and Z. Wen, *Adv. Funct. Mater.*, 2021, **31**, 2101066.
- [S5] X. Hu, G. Zhong, J. Li, Y. Liu, J. Yuan, J. Chen, H. Zhan and Z. Wen, *Energy Environ. Sci.*, 2020, **13**, 2431-2440.
- [S6] J. Ruan, F. Mo, Z. Chen, M. Liu, S. Zheng, R. Wu, F. Fang, Y. Song and D. Sun, *Adv. Energy Mater.*, 2020, **10**, 1904045.
- [S7] H. Tong, C. Wang, J. Lu, S. Chen, K. Yang, M. Huang, Q. Yuan and Q. Chen, *Small*, 2020, **16**, 2002771.
- [S8] B. Fan, J. Yan, A. Hu, Z. Liu, W. Li, Y. Li, Y. Xu, Y. Zhang, Q. Tang, X. Chen and J. Liu, *Carbon*, 2020, **164**, 1-11.
- [S9] J. Wang, H. Fan, Y. Shen, C. Li and G. Wang, *Chem. Eng. J.*, 2019, **357**, 376-383.
- [S10] W. Zhang, Z. Cao, W. Wang, E. Alhajji, A. Emwas, P. Costa, L. Cavallo and H. N. Alshareef, *Angew. Chem. Int. Ed.*, 2020, **59**, 4448-4455.
- [S11] H. Liu, H. Du, W. Zhao, X. Qiang, B. Zheng, Y. Li, B. Cao, *Energy Stor.*

Mater., 2021, **40**, 490-498.

[S12] A. Mahmood, S. Li, Z. Ali, H. Tabassum, B. Zhu, Z. Liang, W. Meng, W. Aftab, W. Guo, H. Zhang, M. Yousaf, S. Gao, R. Zou and Y. Zhao, *Adv. Mater.*, 2019, **31**, 1805430.

[S13] Y. Yi, J. Li, W. Zhao, Z. Zeng, C. Lu, H. Ren, J. Sun, J. Zhang and Z. Liu, *Adv. Funct. Mater.*, 2020, **30**, 2003039.

[S14] K. Zhang, Q. He, F. Xiong, J. Zhou, Y. Zhao, L. Mai and L. Zhang, *Nano Energy*, 2020, **77**, 105018.

[S15] S. Zeng, X. Chen, R. Xu, X. Wu, Y. Feng, H. Zhang, S. Peng and Y. Yu, *Nano Energy*, 2020, **73**, 104807.